ACS NANO
Cite This: ACS Nano 2017, 11, 11250-11263
www.acsnano.org

ARTICLE

Balancing Bacteria–Osteoblast Competition through Selective Physical Puncture and Biofunctionalization of ZnO/Polydopamine/Arginine-Glycine-Aspartic Acid-Cysteine Nanorods

Jun Li,[†,#] Lei Tan,[†,#] Xiangmei Liu,[†] Zhenduo Cui,[‡] Xianjin Yang,[‡] Kelvin Wai Kwok Yeung,[§] Paul K. Chu,[∥] and Shuilin Wu*[,†,‡]

[†]Hubei Collaborative Innovation Center for Advanced Organic Chemical Materials, Ministry-of-Education Key Laboratory for the Green Preparation and Application of Functional Materials, Hubei Key Laboratory of Polymer Materials, School of Materials Science & Engineering, Hubei University, Wuhan 430062, China

[‡]School of Materials Science & Engineering, Tianjin University, Tianjin 300072, China

[§]Department of Orthopaedics & Traumatology, Li Ka Shing Faculty of Medicine, The University of Hong Kong, Pokfulam, Hong Kong, China

[∥]Department of Physics and Department of Materials Science and Engineering, City University of Hong Kong, Tat Chee Avenue, Kowloon, Hong Kong, China

Supporting Information

ABSTRACT: **Bacterial infection and lack of bone tissue integration are two major concerns of orthopedic implants. In addition, osteoinductivity often decreases and toxicity may arise when antibacterial agents are introduced to increase the antibacterial ability. Here hybrid ZnO/polydopamine (PDA)/arginine-glycine-aspartic acid-cysteine (RGDC) nanorod (NR) arrays are designed and prepared on titanium (Ti) implants to not only enhance the osteoinductivity but also effectively kill bacteria simultaneously, which are ascribed to the selective physical puncture and the biofunctionalization of ZnO/PDA/RGDC nanorods during the competition between bacteria and osteoblasts. That is, owing to the much larger size of osteoblasts than bacteria, the hybrid NRs can puncture bacteria but not damage osteoblasts. Meanwhile, the cytocompatibility can be enhanced through the suppression of both reactive oxygen species and higher Zn^{2+} concentration by the covering of PDA and RGDC. The *in vitro* results confirm the selective puncture of the bacterial membrane and the better osteoinductivity. *In vivo* tests also show much higher antibacterial efficacy of the hybrid NRs with far less amounts of lobulated neutrophils and adherent bacteria in the surrounding tissues. In addition, the hybrid NRs also accelerate formation of new bone tissues (20.1% higher than pure Ti) and osteointegration between implants and newly formed tissues (32.0% higher than pure Ti) even in the presence of injected bacteria. This work provides a surface strategy for designing implants with desirable ability of osseointegration and infection prevention simultaneously, which will exhibit tremendous clinical potential in orthopedic and dental applications.**

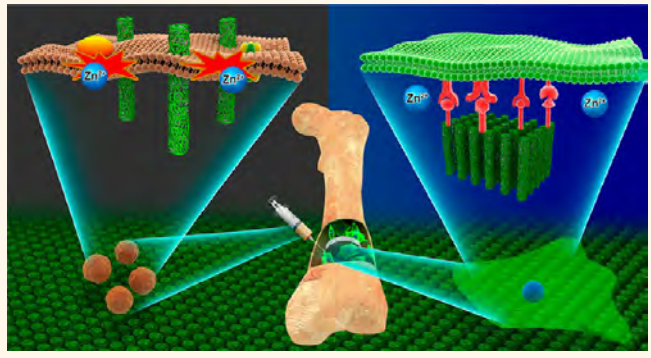

KEYWORDS: *implants, antibacterial, osseointegration, ZnO nanorod, physical puncture*

There are two major postsurgical complications after orthopedic implantation, namely, infection and insufficient bone tissue integration, and, consequently, implant loosening, fracture malunion or nonunion, and failure of the implants may result.[1−5] Infection is commonly caused by

Received: August 8, 2017
Accepted: October 19, 2017
Published: October 19, 2017

DOI: 10.1021/acsnano.7b05620
ACS Nano 2017, 11, 11250–11263

Scheme 1. Schematic illustration of balancing the bacteria−osteoblast competition on titanium modified with ZnO/PDA/RGDC hybrid NR arrays *in vivo*.

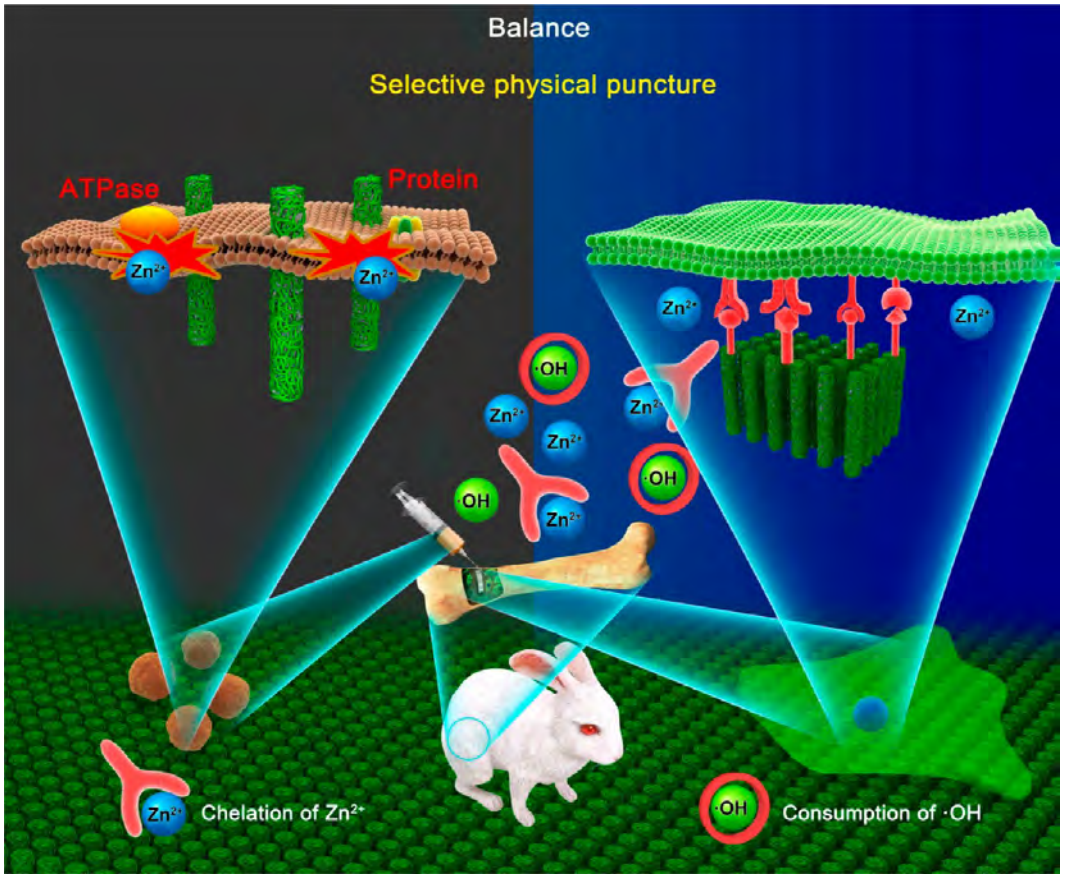

bacteria adhesion and biofilm formation on the implant surface. Being able to resist the host defense and antibiotics,[6] a mature bacterial biofilm can render conventional therapies based on systemic antibiotics ineffective because it has enhanced tolerance to antibiotics and resists phagocytosis and other components in the body's defense system.[5,7,8] In severe cases, a second surgery is required to remove the implants, increasing not only patient trauma but also health costs.[5,9] Therefore, it is necessary to endow artificial implant materials with effective self-antibacterial ability, and various strategies such as antibiotic-loaded architectures, antimicrobial peptides, silver nanoparticles, and so on have been proposed.[5,9,10]

Besides bacterial infection, inadequate bone tissue integration, or osseointegration, is another problem plaguing orthopedic and dental implants.[5,11] Bioactive moieties including growth factors, peptides, proteins, and ions have been used to modify metallic implants to promote implant−bone interactions by stimulating osteogenic differentiation to accelerate interfacial bone regeneration.[5,11] However, the self-antibacterial ability and biocompatibility are sometimes contradictory because cytotoxicity is often associated with the antibacterial ability. Therefore, the key point is to allow sufficient osteoblast growth while inhibiting bacteria, that is, balancing the race between bacteria and osteoblasts. The adhesion of cells and bacteria can be modulated by surface topography through different structures.[12,13] Because osteoblasts are roughly larger than bacteria by over an order of magnitude in size, osteoblasts and bacteria exhibit a great difference in the sensitivity to NR arrays.

The surface of biomaterial incorporated with proper zinc can stimulate initial cell adhesion, spreading, proliferation, osteogenic differentiation, bone formation, and mineralization *in vitro* and *in vivo*.[14−22] Although it has been reported that nanostructured ZnO has good antibacterial activity,[23−28] there is obvious cytotoxicity because a large concentration of Zn^{2+} produces adverse effects on cell growth and tissue formation, and reactive oxygen species (ROS) can induce cell apoptosis.[29−36] Hence, it is critical to control the release of Zn^{2+} and generation of ROS of nanostructured ZnO to balance antibacterial activity and cytotoxicity. Polydopamine (PDA), an important platform and stabilization agent in the fabrication of diverse organic−inorganic materials with specific functionalities, has excellent biocompatibility, biodegradation, and hydrophilicity.[37,38] In addition, PDA has a strong antioxidant effect to scavenge reactive free radicals.[38] The reaction between PDA and amine- and/or thiol-containing molecules favors grafting of bioactive molecules.[37,38] Similar to arginine-glycine-aspartic acid (RGD), RGD-cysteine (RGDC) is effective in improving attachment of many types of cells onto different substrates and can engage and activate integrin adhesion receptors on cells.[39] Therefore, covalent immobilization of RGDC peptide is a viable strategy to improve cell adhesion and proliferation to enhance the osteogenic properties.[40−43]

Herein, we describe a hybrid of ZnO/PDA/RGDC nanorods (NRs) that is designed to balance the antibacterial activity and cytotoxicity of biomedical implants through selective physical puncture by hybrid ZnO NRs and the biofunctionalization of ZnO/PDA/RGDC nanorods. The mechanism of balancing the

DOI: 10.1021/acsnano.7b05620
ACS Nano 2017, 11, 11250−11263

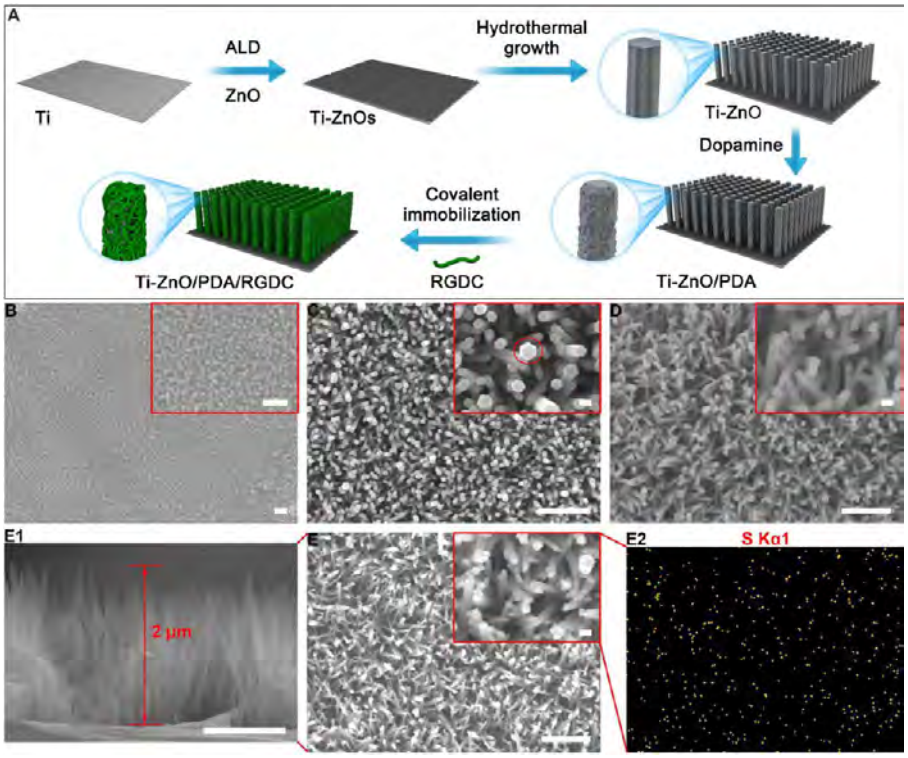

Figure 1. (A) Schematic illustration of the fabrication process of the hybrid ZnO/PDA/RGDC NR arrays on Ti; FE-SEM images of (B) Ti-ZnOs (scale bars = 100 nm), (C) Ti-ZnO, (D)Ti-ZnO/PDA, and (E) Ti-ZnO/PDA/RGDC; (E1) cross-sectional image of Ti-ZnO/PDA/RGDC; (E2) elemental mapping of Ti-ZnO/PDA/RGDC (scale bars = 100 nm (inset figures = 1 μm)).

bacteria−osteoblast race on Ti modified with ZnO/PDA/RGDC hybrid NR arrays *in vivo* is schematically illustrated in Scheme 1. The ZnO NR arrays are modified by self-polymerization of dopamine and covalent immobilization of RGDC peptide, which is shown in Figure 1A, and the details of sample names are summerized in Table S1. The biocompatibility can be improved by reducing the amount of ROS produced by ZnO through the radical scavenging of PDA. In addition, the release concentration of Zn^{2+} can be reduced *via* the chelation between PDA and Zn^{2+}, further enhancing the biocompatibility. The *in vitro* and *in vivo* results suggest that the hybrid NR arrays possess effective self-antibacterial activity against adherent *S. aureus* and *E. coli* as well as outstanding osteogenic properties even in the presence of injected bacteria.

RESULTS AND DISCUSSION

Morphology and Structure. The ZnO seed layer (ZnOs) prepared by atomic layer deposition (ALD) has uniform and narrow particles with an average size of 20 nm (Figure 1B), and the thickness of this layer is approximately 40 nm (Figure S1). As shown in Figure 1C, the ZnO NRs exhibit a highly uniform density and even spatial distribution. Most of ZnO NRs grow along the near-perpendicular direction to the Ti substrate. The inset image in Figure 1C reveals hexagonal rods (marked by a red circle) with an average diameter of 100 nm. The deposition of PDA leads to a relatively rough surface morphology, and the hexagonal NRs disappear (Figure 1D) since the PDA film covers the ZnO NRs. After covalent immobilization of RGDC peptide (Figure 1E), the ZnO/PDA/RGDC NRs have an average length of approximately 2 μm (Figure 1E1). The elemental mapping image of Ti-ZnO/PDA/RGDC (Figure 1E2) corresponding to the inset area in Figure 1E shows an even distribution of sulfur, thereby confirming the uniform distribution of RGDC on the surface. The typical ZnO NR has a diameter of about 100 nm and length of 2 μm, and the selected area electron diffraction (SAED) pattern reveals a single-crystal hexagonal structure (Figure S2A).[28] The morphology of Ti-ZnO/PDA and Ti-ZnO/PDA/RGDC is shown in Figure S2B,C, respectively, the thickness of the PDA layer is around 7−10 nm after self-polymerization, and the modified RGDC does not change the thickness of layers.

Figure 2A shows the X-ray diffraction (XRD) patterns of Ti, Ti-ZnOs, Ti-ZnO, Ti-ZnO/PDA, and Ti-ZnO/PDA/RGDC. Ti-ZnO, Ti-ZnO/PDA, and Ti-ZnO/PDA/RGDC exhibit diffraction peaks of (0 0 2), (1 0 3), and (2 0 2) in accordance with the hexagonal wurtzite phase of ZnO.[44,45] The dominant diffraction peak at 34.4° is indexed to the (0 0 2) plane of the wurtzite structure of ZnO, suggesting that the ZnO NRs grow preferentially along the [0001] direction.[44,46−48] Ti-ZnO/PDA and Ti-ZnO/PDA/RGDC show similar XRD patterns to Ti-ZnO, indicating that grafting of PDA and RGDC does not alter the phase structure of the ZnO NRs.

Figure 2B shows broad peaks at 3432 and 3363 cm^{-1} in the FTIR spectra of Ti-ZnO/PDA and Ti-ZnO/PDA/RGDC arising from amine N−H and O−H stretching, respectively.[49,50]

The peak at 2924 cm^{-1} corresponds to aliphatic C−H stretching of CH_2,[49] and that at 1626 cm^{-1} can be ascribed to the overlap of C═C resonance vibration in the aromatic ring. The C−C, C−O, and C−N regions are in the range between 1200 and 1500 cm^{-1}.[51] The characteristics are similar to those in the spectrum of pure PDA (Figure S3A).[49,50] After modification with the RGDC peptide, a broad peak at 1682 cm^{-1} corresponding to the amide bond I of the peptide ligand appears.[52,53] The peak at 2590−2550 cm^{-1} associated with stretching of the S−H bond disappears, indicating that the

DOI: 10.1021/acsnano.7b05620
ACS Nano 2017, 11, 11250−11263

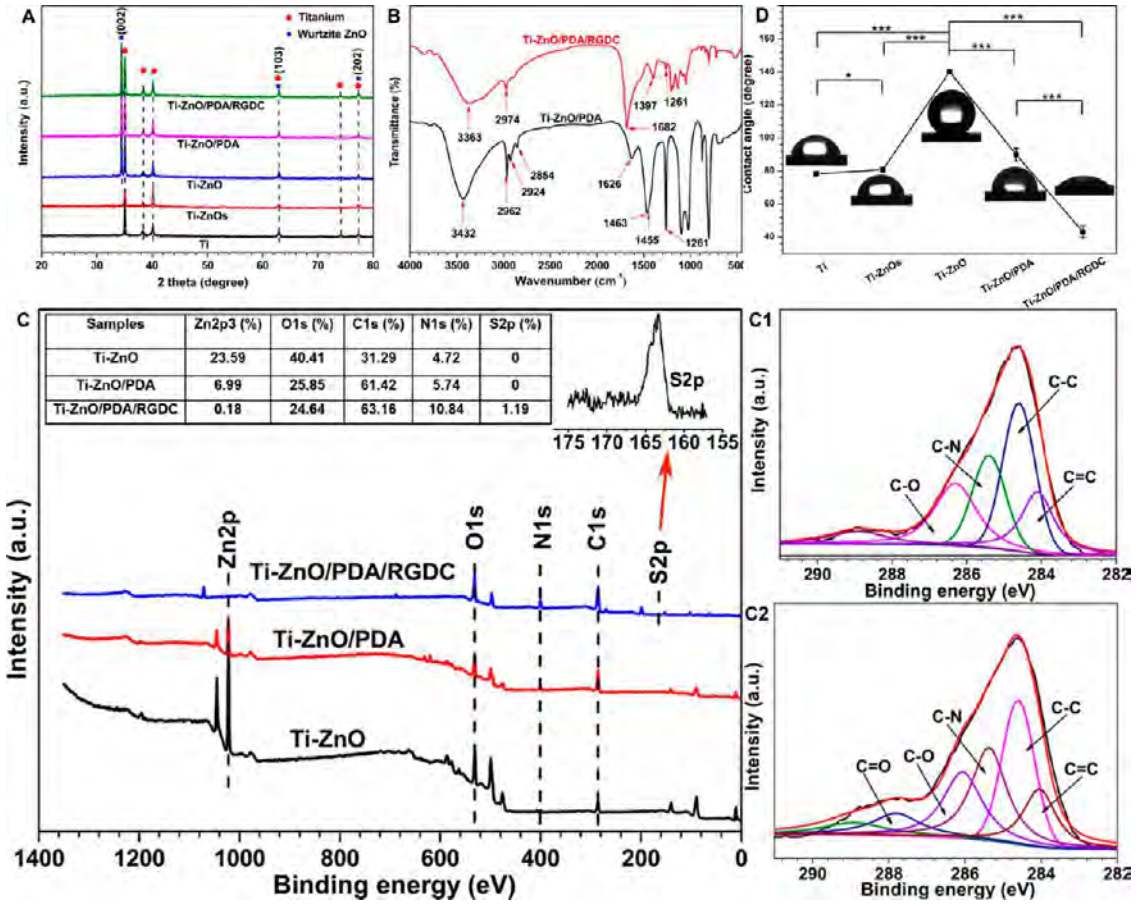

Figure 2. (A) XRD patterns of Ti, Ti-ZnOs, Ti-ZnO, Ti-ZnO/PDA, and Ti-ZnO/PDA/RGDC; (B) FTIR spectra of Ti-ZnO/PDA and Ti-ZnO/PDA/RGDC; (C) XPS survey spectra of Ti-ZnO, Ti-ZnO/PDA, and Ti-ZnO/PDA/RGDC; elemental chemical composition and ratio and S 2p peak of Ti-ZnO/PDA/RGDC, (C1) C 1s peak of Ti-ZnO/PDA, (C2) C 1s peak of Ti-ZnO/PDA/RGDC; (D) water contact angles and photographs of water droplets on Ti, Ti-ZnOs, Ti-ZnO, Ti-ZnO/PDA, and Ti-ZnO/PDA/RGDC. The error bars indicate means ± standard deviations: *$P < 0.05$ and ***$P < 0.001$ (t test).

RGDC molecules (Figure S3B) are covalently grafted onto PDA because catechols in PDA can react with thiols and amines in RGDC *via* Michael addition or Schiff base reactions.[37,38] These results show that RGDC is immobilized on the PDA-functionalized ZnO NRs, and the covalent mechanism is schematically illustrated in Figure S4.

The survey X-ray photoelectron spectroscopy (XPS) spectrum (Figure 2C) indicates that Ti-ZnO, Ti-ZnO/PDA, and Ti-ZnO/PDA/RGDC contain Zn, C, N, O, and S (inserted table). As shown in Figure 2C1,2, the C 1s peaks of Ti-ZnO/PDA and Ti-ZnO/PDA/RGDC can be deconvoluted into five subpeaks at 284.1, 284.6, 285.4, 286.3, and 287.7 eV corresponding to C═C, C−C, C−N/C-S, C−O, and C═O, respectively.[54] The PDA-functionalized ZnO NRs show larger N 1s content from 4.72% to 5.74% and smaller O 1s content from 40.41% to 25.85% compared to Ti-ZnO (Figure 2C). The nitrogen-to-carbon (N/C) ratio of 0.093 is close to the theoretical N/C of 0.125 for dopamine,[37,55] implying that Ti-ZnO is modified with PDA. Immobilization of RGDC is confirmed by the larger N 1s peak from 5.74% to 10.84% and S content from 0% to 1.19% compared to Ti-ZnO/PDA. Sulfur is only observed from Ti-ZnO/PDA-RGDC (Figure 2C). The result reveals that PDA and RGDC are immobilized onto the Ti-ZnO substrate. Physical adsorption *via* weak noncovalent bonds is unable to provide long-term bioactivity, leading to low stability, molecular leakage, and uncontrolled desorption of biomolecules in the physiological environment.[11,42,52] In comparison, strong anchoring of RGDC peptides on the surface by covalent immobilization is more stable, resulting in better cell attachment.

As shown in Figure 2D, the polished Ti substrate shows a contact angle of 78.3 ± 1.1°. It is 80.7 ± 1.5° for Ti-ZnOs, while after hydrothermal growth of the ZnO NR arrays, this value increases to 140.2 ± 1.2°. There are two main factors regulating the surface wettability of ZnO NR arrays: surface roughness and surface free energy.[56] After coating with PDA, the contact angle decreases to 89.9 ± 3.9°,[38] and since RGDC molecules have a hydrophilic nature,[52] the contact angle on Ti-ZnO/PDA/RGDC diminishes to 43.1 ± 3.5°. Hence, PDA and RGDC improve the wettability of the ZnO NRs surface, converting it from being hydrophobic to being hydrophilic without altering the morphology of the ZnO NR arrays significantly. Wettability is an important property of biomaterials because cell attachment, osteoblast differentiation, bone formation, and so on are more likely to occur on hydrophilic surfaces.[57,58]

***In Vitro* Zn Ion Release Behavior and Related Mechanisms.** As shown in Figure 3A, the trend of Zn^{2+} released from Ti-ZnO, Ti-ZnO/PDA, and Ti-ZnO/PDA/RGDC is similar. The release is rapid in the first 9 days and slows/stabilizes in subsequent months. In fact, Zn^{2+} release lasts up to 90 days without initial burst release. As shown in Figure

DOI: 10.1021/acsnano.7b05620
ACS Nano 2017, 11, 11250−11263

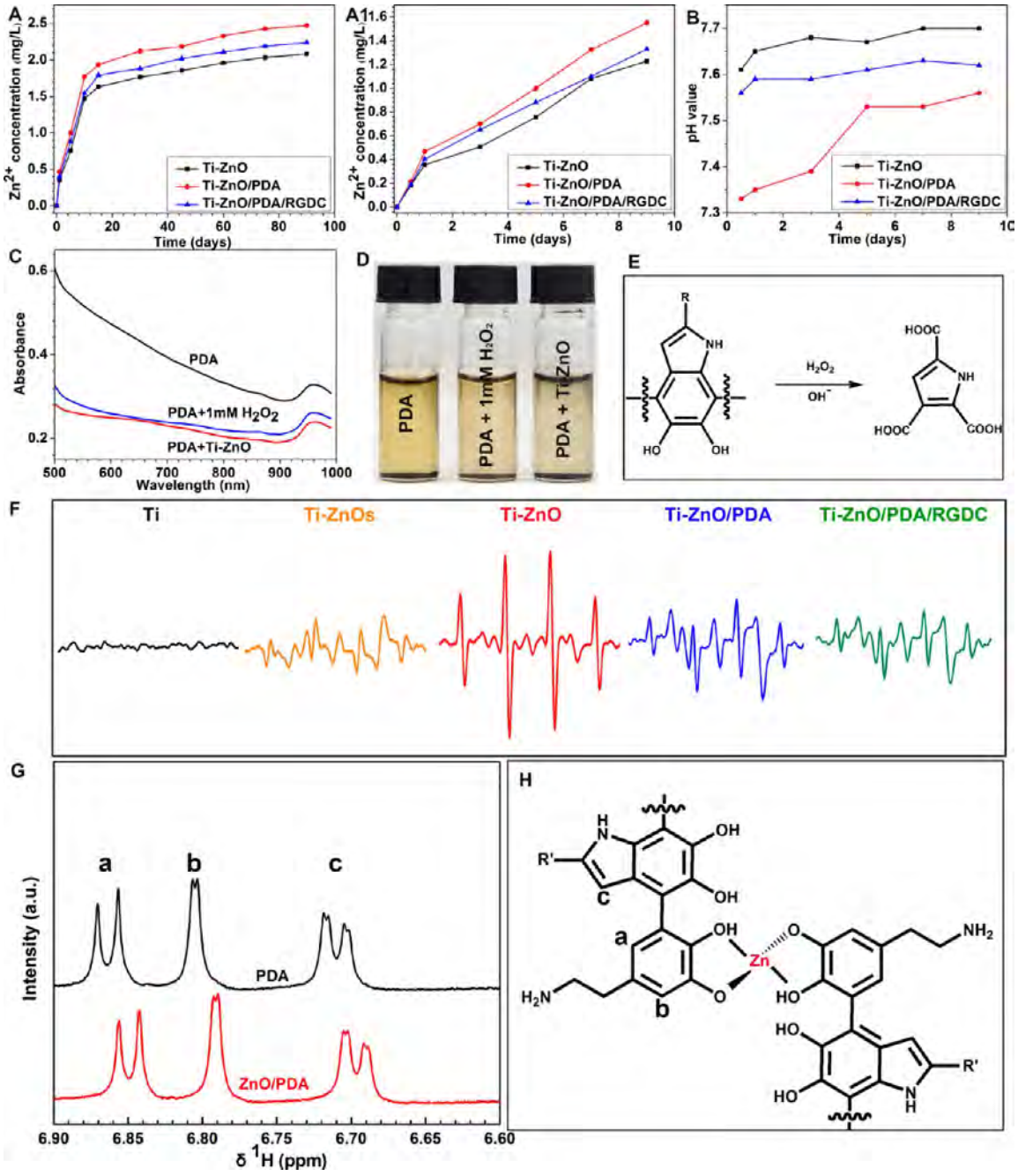

Figure 3. (A) Cumulative zinc ion release curves of Ti-ZnO, Ti-ZnO/PDA, and Ti-ZnO/PDA/RGDC after immersion at 37 °C for 90 days; (A1) short-term release; (B) pH values of the liquids corresponding to A1. Degradation of PDA: (C) UV−vis absorption spectra, (D) corresponding photograph, (E) chemical degradation pathway of PDA by H_2O_2 (chemical formula of R group presented in Figure S5); (F) ESR spectra of Ti, Ti-ZnOs, Ti-ZnO, Ti-ZnO/PDA, and Ti-ZnO/PDA/RGDC; (G) ^{1}H NMR spectra of PDA and PDA/ZnO; (H) structure of the Zn-PDA complex.

3A1, the cumulative released Zn^{2+} concentrations from Ti-ZnO, Ti-ZnO/PDA, and Ti-ZnO/PDA/RGDC after 9 days are 1.229, 1.5513, and 1.33 mg/L, respectively. Owing to the modification with PDA and RGDC, Ti-ZnO is expected to show faster Zn^{2+} release than Ti-ZnO/PDA and Ti-ZnO/PDA/RGDC, but Ti-ZnO/PDA shows the largest Zn release under the same conditions during incubation for 90 days, and the mechanism will be discussed later in the paper.

As aforementioned, PDA has a strong antioxidant effect to scavenge significantly ROS. Figure 3B shows the pH of the liquids corresponding to Figure 3A1. As shown in Figure 3A1 and B, the Zn release rate increases with decreasing pH. Hence, a more acidic condition accelerates the dissolution of ZnO, inducing faster release of Zn^{2+}. The acidity is increased due to oxidation-induced degradation of PDA, which can be caused by generation of ROS and formation of carboxylic acid. As shown in Figure 3C and D, PDA loses its absorbance in the presence of Ti-ZnO, and this process is accompanied by color fading. When PDA is treated with 1 mM H_2O_2 as a positive control, ROS such as $^{\bullet}OH$ can be generated from the surface of ZnO, and generation of ROS will be discussed in the following section.[26−28] After incubation with H_2O_2, PDA undergoes

DOI: 10.1021/acsnano.7b05620
ACS Nano 2017, 11, 11250−11263

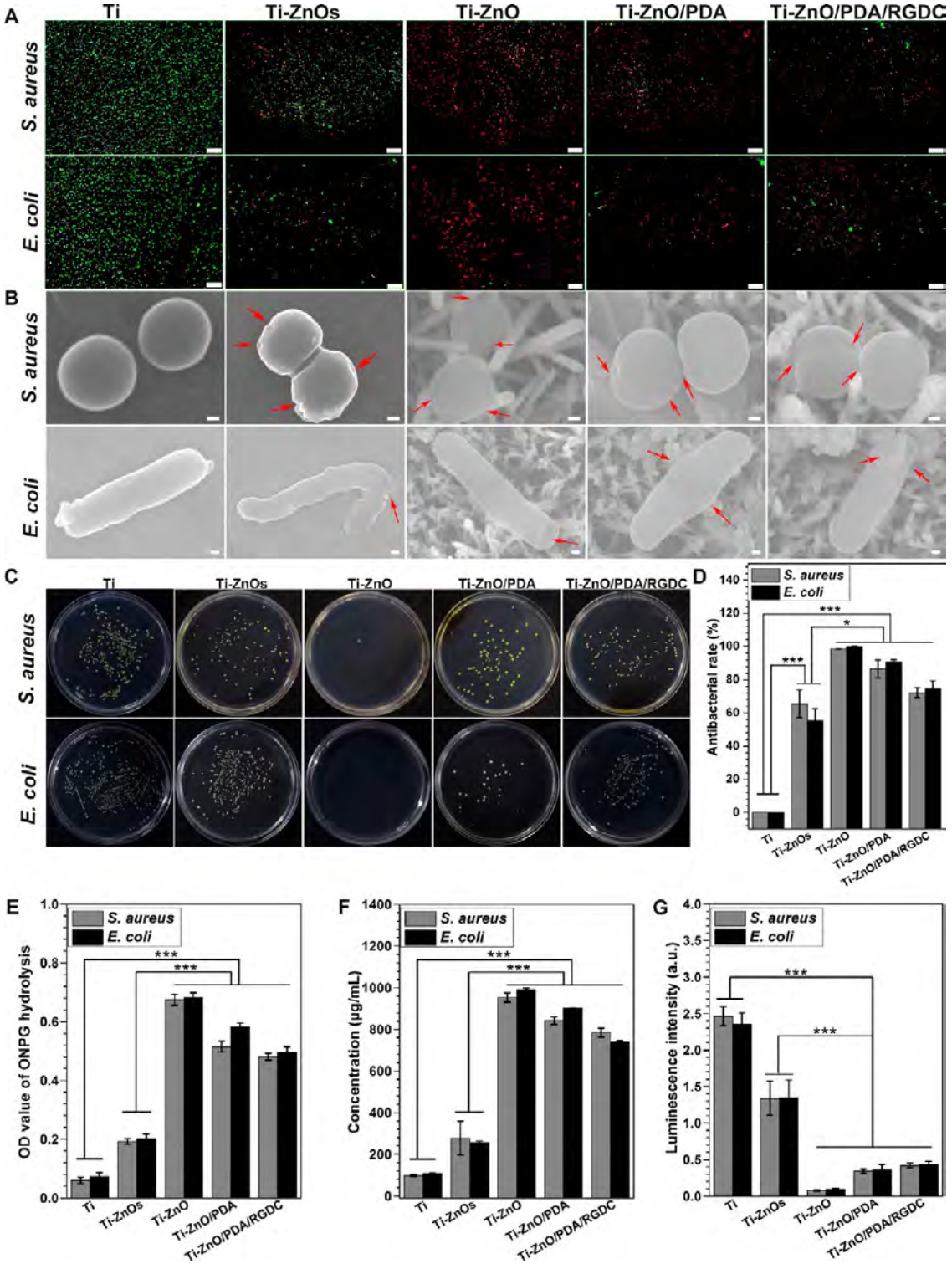

Figure 4. (A) Fluorescent images of stained bacteria after treatment on various surfaces for *S. aureus* and *E. coli* (scale bars = 50 μm); (B) FE-SEM morphology of *S. aureus* and *E. coli* seeded on the various surfaces (scale bars = 100 nm). Antibacterial activity of the different samples through recultivated bacterial colonies on agar culture plates: (C) *S. aureus* and *E. coli* seeded on various surfaces at a concentration of 10^7 CFU/mL; percentage reduction: (D) *S. aureus* and *E. coli* recultured on agar after dissociation from the various surfaces. (E) Permeability of bacterial membrane determined by ONPG hydrolysis assay. (F) Protein leakage analysis and (G) level of ATP from *E. coli* and *S. aureus* treated with different samples. The error bars indicate means ± standard deviations: $^*P < 0.05$ and $^{***}P < 0.001$ (*t* test).

oxidation-induced degradation, forming carboxylic acid compounds as shown in Figure 3E (the chemical formula of the R group is presented in Figure S5A).[38,59,60] In this process, PDA consumes a part of •OH.

ESR (electron spin resonance) with spin trapping is an effective technique to identify and quantify short-lived free radicals such as the hydroxyl radical (•OH), which can be used to monitor generation of ROS in aqueous suspensions of nano

DOI: 10.1021/acsnano.7b05620
ACS Nano 2017, 11, 11250−11263

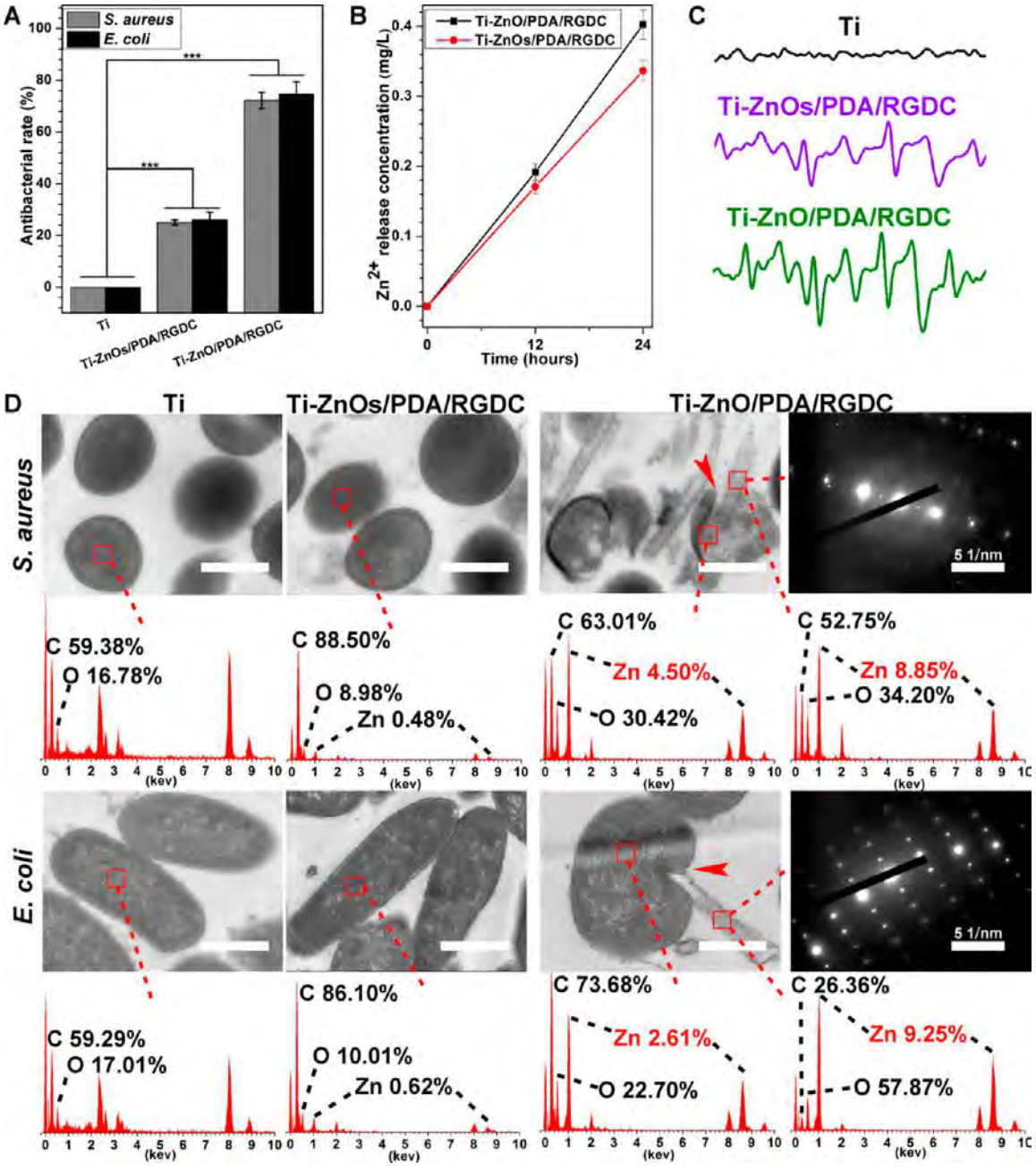

Figure 5. Antibacterial activity of Ti-ZnOs/PDA/RGDC and Ti-ZnO/PDA/RGDC through percentage reduction: (A) *S. aureus* and *E. coli* recultured on agar after dissociation from the various surfaces. (B) Cumulative zinc ion release curves of Ti-ZnOs/PDA/RGDC and Ti-ZnO/PDA/RGDC after immersion at 37 °C for 1 day. (C) ESR spectra of Ti, Ti-ZnOs/PDA/RGDC, and Ti-ZnO/PDA/RGDC. (E) TEM images of ultrathin section (about 70 nm) and the corresponding EDS of *S. aureus* and *E. coli* treated with Ti, Ti-ZnOs/PDA/RGDC, and Ti-ZnO/PDA/RGDC (scale bars = 500 nm). The error bars indicate means ± standard deviations: ***$P < 0.001$ (t test).

ZnO. 5,5-Dimethyl-1-pyrroline *N*-oxide (DMPO) is used to verify generation of •OH and reaction with •OH to produce DMPO-OH with a characteristic ESR spectrum of four lines of 1:2:2:1.[35,36] The peak intensity is proportional to the ROS level, and generation of •OH by the nanometer-scale ZnO can be ascribed to the high surface-to-volume ratio.[35,36] The wet surface on ZnO NRs has numerous defect sites and empty oxygen sites (oxygen vacancies), which can trap electrons.[35] As shown in Figure 3F, Ti-ZnO has the largest number of •OH, whereas Ti-ZnOs possesses the least number of •OH in the experimental groups. Surface modification of ZnO NRs with PDA and RGDC reduces significantly the amount of •OH compared to Ti-ZnO. The PDA-functionalized ZnO NRs can form carboxylic acid compounds, and this change consumes a part of •OH produced by the ZnO NRs. Overproduction of ROS generation can disrupt the cell membrane and induce oxidative stress to cause leakage of cytoplasmic contents and damage DNA as well as cellular proteins, leading to cell death.[35,61] In addition, tiny ROS have no negative effect on physiological functions of cells.[61] Therefore, the cytotoxicity of hybrid NR arrays will be minimized due to the comsuption of the majority of ROS.

Coordination between Zn^{2+} and PDA exists on the hybrid NR arrays. In order to elucidate the mechanism, the ^{1}H NMR

DOI: 10.1021/acsnano.7b05620
ACS Nano 2017, 11, 11250−11263

spectra are shown in Figure 3G. The resonance of protons on pyrocatechol shifts upfield by about 0.01 ppm (*i.e.*, a, b, c peaks in Figure 3G), suggesting that coordination occurrs on the chelated site of pyrocatechol.[62] The proposed structure of the Zn-PDA complex is displayed in Figure 3H (the chemical formula of the R′ group is presented in Figure S5B). PDA, an efficient absorbent to remove Zn ions from the environment or a living body, can bind to Zn^{2+} *via* chelation. As mentioned above, a large concentration of Zn^{2+} can produce adverse effects affecting cell growth and tissue formation.[31−34] The biofunctionalization of ZnO/PDA/RGDC nanorods presents antibacterial activity and osteogenic properties. In this respect, chelation can modulate the bioavailability of the released Zn^{2+} to control the biocompatibility of both Ti-ZnO/PDA and Ti-ZnO/PDA/RGDC.

Antibacterial Activity *in Vitro*. The bacteria viability is qualitatively evaluated by the live/dead (green/red) staining assay, and the corresponding fluorescent images are shown in Figure 4A. Compared to pure Ti, the surface coverage on the modified samples is significantly lower, suggesting an antiadhesion effect of hybrid NRs on *S. aureus* and *E. coli*. Moreover, more red spots can be observed from Ti-ZnOs, Ti-ZnO, Ti-ZnO/PDA, and Ti-ZnO/PDA/RGDC, indicating more dead bacteria and fewer living bacteria. Ti-ZnO shows no green spots and the best antibacterial ability. Furthermore, the morphology of the adherent *S. aureus* and *E. coli* after incubation for 12 h is examined by field emission scanning electron microscopy (FE-SEM) in Figure 4B. *S. aureus* is spherical on Ti, but irregular or completely lysed on Ti-ZnOs, Ti-ZnO, Ti-ZnO/PDA, and Ti-ZnO/PDA/RGDC surfaces (red arrow). Similarly, compared to *E. coli* on Ti, *E. coli* becomes corrugated and distorted or is even partly lysed on Ti-ZnOs, Ti-ZnO, Ti-ZnO/PDA, and Ti-ZnO/PDA/RGDC (red arrow).

The contact-killing antibacterial activity against adherent *S. aureus* and *E. coli* of Ti, Ti-ZnOs, Ti-ZnO, Ti-ZnO/PDA, and Ti-ZnO/PDA/RGDC is evaluated by the bacteria counting method, in which the adherent bacteria are detached from the samples and recultured on agar plates (Figure 4C). Compared to pristine Ti, Ti-ZnO, Ti-ZnO/PDA, and Ti-ZnO/PDA/RGDC show inhibited growth of bacteria cells in Figure 4D. Ti-ZnOs shows the lowest antibacterial activity with antibacterial rates of 65.5 ± 8.3% against *S. auerus* and 55.4 ± 7.3% against *E. coli*. After hydrothermal growth of the ZnO NR arrays, Ti-ZnOs shows the highest antibacterial effects, with antibacterial rates of 98.7 ± 0.1% against *S. aureus* and 99.9 ± 0.1% against *E. coli*. Ti-ZnO displays greater bacterial killing effeciency than Ti-ZnO/PDA (85.6 ± 5.4% for *S. aureus* and 89.6 ± 1.4% for *E. coli*) and Ti-ZnO/PDA/RGDC (72.2 ± 3.2% for *S. auerus* and 74.7 ± 4.8% for *E. coli*). The results of the bacteria counting analyses are consistent with live/dead staining discussed above. The contact-killing of bacteria can be further confirmed through examining the bacterial membrane penetrability using *o*-nitrophenyl-*β*-D-galactopyranoside (ONPG). ONPG can penetrate the bacterial membrane and react with the intracellular enzyme *β*-D-galactosidase to form yellow-colored *o*-nitrophenol when the bacterial membrane is damaged.[63] The permeability of the bacterial membrane significantly increases after exposure to Ti-ZnO, Ti-ZnO/PDA, and Ti-ZnO/PDA/RGDC (Figure 4E). Simultaneously, the protein leakage and adenosine triphosphate (ATP) level from bacteria show the same trendency as the permeability of the bacterial membrane (Figure 4F and G), indicating that the antibacterial activity of Ti-ZnO, Ti-ZnO/PDA, and Ti-ZnO/PDA/RGDC against *S. aureus* and *E. coli* results from bacterial membrane damage, protein leakage, and the decrease in ATP level.

Antibacterial Mechanism. The above results reveal that the contact-killing antibacterial activity of Ti-ZnO/PDA and Ti-ZnO/PDA/RGDC against adherent bacteria and the antibacterial rate decreases slightly compared to the uncoated ZnO NRs. The antibacterial mechanisms of ZnO NRs have three aspects.[26−28,35] (a) ROS (Figure 3F) such as $^{\bullet}OH$ are generated and two OH radicals can be recombined to form hydrogen peroxide (H_2O_2), which disrupts the cell membrane (Figure 4E), causing leakage of cytoplasmic contents (Figure 4F and G), DNA damage, and cell death. (b) Zinc ions (Figure 3A) from the ZnO NRs can penetrate cell membranes (Figure 4E) to inhibit active transport and metabolism of sugar and disrupt metal ion homeostasis and enzyme systems when the concentration reaches a specific level. (c) ZnO NRs penetrate the bacterial cell wall, inducing loss of membrane integrity and subsequent death. The vertically aligned structure of the ZnO NR arrays with a diameter less than 100 nm provides fewer anchoring sites and reduces the contact area between the materials surface. So the cell wall of bacteria can be physically punctured. However, the PDA-functionalized ZnO NRs can decrease the amount of $^{\bullet}OH$ compared to Ti-ZnO (Figure 3B to F). Furthermore, PDA can bind with Zn^{2+} (Figure 3G and H), and the bioavailability of Zn^{2+} can be decreased to reduce the toxicity. As a result, the antibacterial rate decreases slightly after surface modification of ZnO NRs with PDA and RGDC, implying that the physical puncture of bacteria by hybrid NR arrays should be predominant.

To prove the antibacterial mechanism of hybrid NR arrays, Ti-ZnOs/PDA/RGDC and Ti-ZnO/PDA/RGDC are compared. The amounts of *S. aureus* on Ti-ZnOs/PDA/RGDC and Ti-ZnO/PDA/RGDC are reduced by 25.1 ± 1.2% and 72.2 ± 3.2%, respectively, and those of *E. coli* decrease by 26.0 ± 2.9% and 74.7 ± 4.8%, respectively (Figure 5A and Figure S6). Furthermore, the trendency of Zn^{2+} release (Figure 5B) and the generation of ROS (Figure 5C) from Ti-ZnOs/PDA/RGDC and Ti-ZnO/PDA/RGDC are similar, suggesting that Zn^{2+} release and generation of ROS have small antimicrobial efficiency, and the physical puncture by the Ti-ZnO/PDA/RGDC plays a predominant role in contact-killing antibacterial activity against adherent bacteria, which can be proven by the section of bacteria cultured on the surface of samples. As shown in Figure 5D, in the case of both Ti and Ti-ZnOs/PDA/RGDC groups, TEM images show the normal structures of bacteria, *i.e.*, regular shapes with intact bacterial membrane. Energy dispersive spectroscopy (EDS) detection shows no signal of Zn in bacteria on pure Ti, while a small amount of Zn^{2+} penetrates into the bacteria on Ti-ZnOs/PDA/RGDC. This is why the former has no antibacterial activity, while the latter exhibits antibacterial efficacy of 25.1 ± 1.2% and 26.0 ± 2.9% against *S. aureus* and *E. coli*, respectively; that is, the released Zn^{2+} can kill bacteria a little bit. In contrast, the membranes of two kinds of bacteria on Ti-ZnO/PDA/RGDC are severely damaged and have obvious cytoplasm leakage, in accordance with quantitative analysis of protein leakage (Figure 4F and G), which is caused by the direct puncture by needle-like NRs (Figure 5D, red arrows). In addition, EDS spectra show that Zn content in bacteria on Ti-ZnO/PDA/RGDC is higher than that on Ti-ZnOs/PDA/RGDC. This is why Ti-ZnO/PDA/RGDC exhibits much higher antibacterial efficacy than Ti-ZnOs/PDA/RGDC; that is, the synergistic action of both physical puncture

DOI: 10.1021/acsnano.7b05620
ACS Nano 2017, 11, 11250−11263

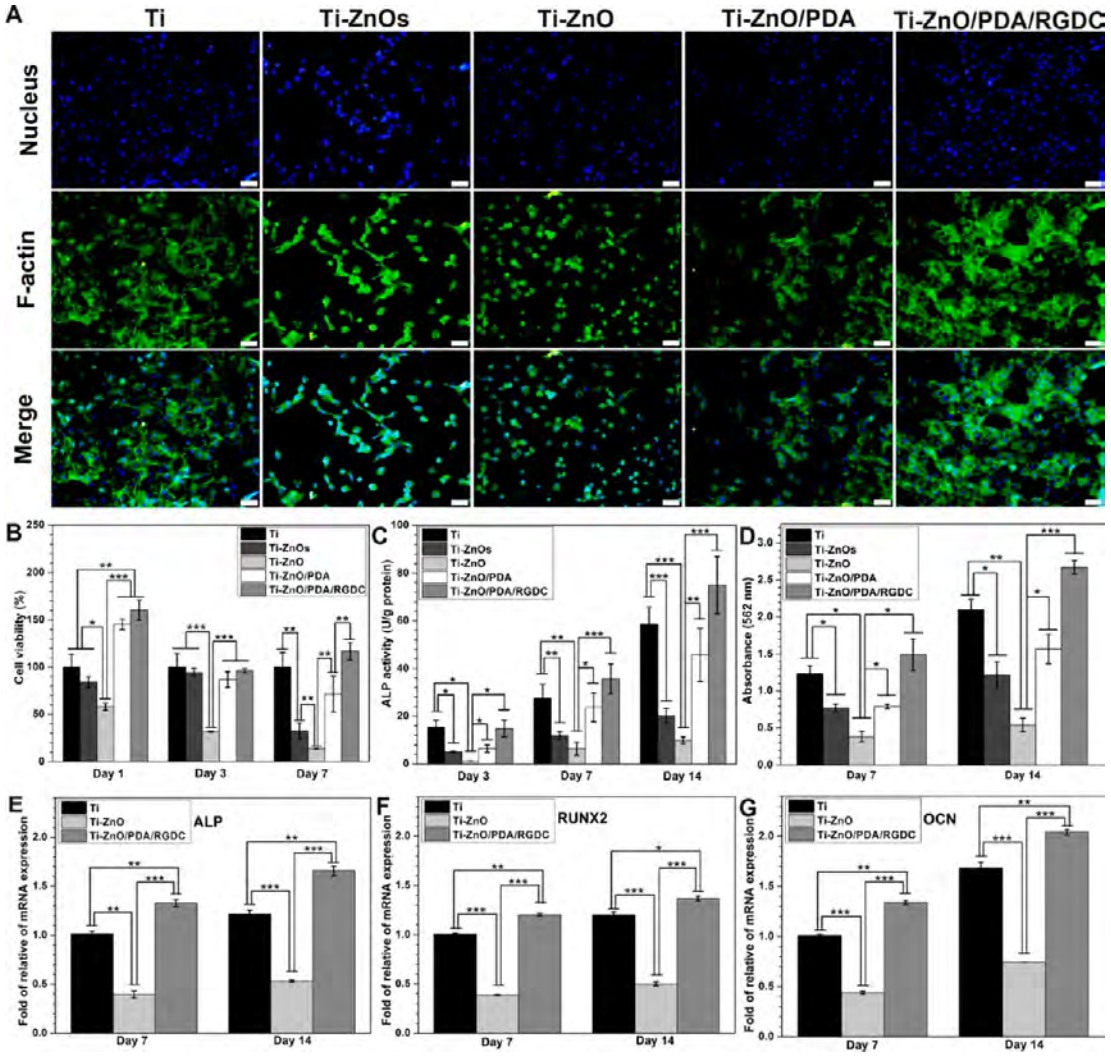

Figure 6. (A) Fluorescent images of MC3T3-El cells cultured on different samples for 24 h with F-actin stained with FITC (green) and nuclei stained with DAPI (blue) (scale bars = 50 μm); (B) MTT assay of cell viabilities cultured in the medium with different samples after 1, 3, and 7 days; (C) specific ALP activities of MC3T3-El osteoblasts cultured in the medium with different samples after 1, 3, and 7 days; (D) quantitative measurement of the Alizarin Red staining after 7 and 14 days; quantification of the osteoblast-related gene expressions of (E) ALP, (F) RUNX2, and (G) OCN on Ti, Ti-ZnO, and Ti-ZnO/PDA/RGDC using normalization against a β-actin reference on the 7th and 14th day. The error bars indicate means ± standard deviations: *P < 0.05, **P < 0.05, and ***P < 0.001 (t test).

by NRs and released Zn^{2+} plays the key role in bacteria-killing. The SAED patterns obtained from these needle-like NRs confirm that they are single crystallized ZnO NRs, which is well in accordance with the pattern shown in Figure S2A. The cross-sectional view also confirms the physical puncture of bacteria by ZnO NRs; that is, both *S. aureus* and *E. coli* are irregular, corrugated, and lysed on the Ti-ZnO/PDA/RGDC surface (Figure S7, red arrows). Osteoblasts and bacteria exhibit a great difference in the sensitivity to NR arrays because osteoblasts are roughly over an order of magnitude larger than bacteria in size. In contrast osteoblasts on Ti-ZnO/PDA/RGDC show excellent cell adherence and abundant cell spreading from the cross-sectional view in Figure S8. *In vitro* cytocompatibility evaluation will be discussed below in detail.

Cell Morphology. As shown in Figure 6A, the cell morphology, cell adhesion, and spreading activity are examined by staining with FITC and DAPI to visualize the F-actin and nuclei, respectively. After culturing for 1 day, the cells spread poorly on Ti-ZnOs and Ti-ZnO, exhibiting a spherical morphology without filopodia extensions. In comparison, Ti-ZnO/PDA promotes cell extension and Ti-ZnO/PDA/RGDC shows improved cell spreading. Most of the cells on Ti-ZnO/PDA/RGDC have a polygonal shape with a large number of filopodia and lamellipodia, suggesting that Ti-ZnO/PDA/RGDC favors growth and proliferation of osteoblasts without appreciable cytotoxicity. Similar to the fluorescent morphology, Ti-ZnOs and Ti-ZnO have low affinity to osteoblasts and the osteoblasts show a spherical morphology (Figure S9), while the attached cells grow well on Ti-ZnO/PDA/RGDC. The polygonal shape reflects good cell adherence and abundant cellular extension, indicating that Ti-ZnO/PDA/RGDC can promote bone cell adhesion and growth.

Cell Viability. Figure 6B shows the viability of MC3T3-E1 osteoblasts on Ti, Ti-ZnOs, Ti-ZnO, Ti-ZnO/PDA, and Ti-ZnO/PDA/RGDC. Throughout the incubation periods (1, 3, and 7 days), Ti-ZnO exhibits the largest cell toxicity with less than 60% viability compared to pure Ti. With the PDA coating, the cell toxicity decreases significantly, and after covalent immobilization of RGDC peptide, the cell viability increases further to a level much higher than pure Ti. Adhesion and

DOI: 10.1021/acsnano.7b05620
ACS Nano 2017, 11, 11250−11263

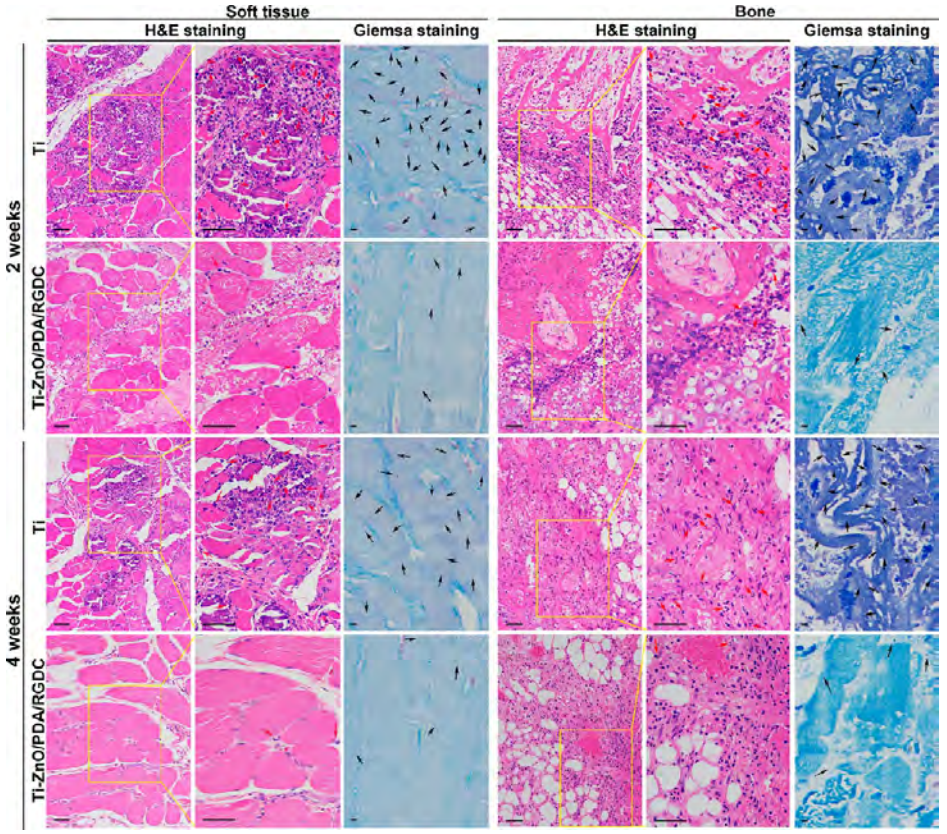

Figure 7. H&E staining (scale bars = 50 μm) and Giemsa (scale bars = 5 μm) staining images showing the infection degree of the soft tissue and bone after 2 weeks and 4 weeks postsurgery.

proliferation of osteoblasts on the ZnO NRs modified by PDA and RGDC are improved compared to bare ZnO NR arrays. After incubation for 3 days, the samples reveal definite cell toxicity compared to pure Ti. As the incubation time is increased, the cell toxicity increases slightly in comparison with the control due to the continuous release of Zn^{2+} (Figure 3A1). In general, Ti-ZnO/PDA/RGDC shows the lowest cell toxicity. To further investigate the cytotoxicity of Zn^{2+} in this concentration range, the final extracted liquid after 1 day was chosen for a control experiment. After 1 day release, the extracted liquids of Ti, Ti-ZnOs, Ti-ZnO, Ti-ZnO/PDA, and Ti-ZnO/PDA/RGDC are cultured with cells for 1 day. As shown in Figure S12, the cell viabilities of Ti, Ti-ZnOs, Ti-ZnO, Ti-ZnO/PDA, and Ti-ZnO/PDA/RGDC are decreased compared to the corresponding results shown in Figure 6B because the final Zn^{2+} concentration of the extracted liquids after 1 day release is maximum for another 1 day incubation. However, the cell viabilities in Ti-ZnO/PDA (82.3%) and Ti-ZnO/PDA/RGDC (87.4%) are still much higher than that in Ti-ZnO (49.1%), confirming that the cytotoxicity of Zn^{2+} of Ti-ZnO can be significantly reduced through combination with PDA. Generation of ROS and the bioavailability as well as toxicity of Zn^{2+} impact the cell viability. Since PDA has a strong antioxidant effect to scavenge significantly ROS, generation of ROS (Figure 3F) is apparently suppressed, and so the cytotoxicity of ZnO is decreased after surface modification with PDA. Moreover, tiny ROS have no negative effect on physiological functions of cells.[61] In addition, an excess concentration of Zn^{2+} can produce adverse effects on cell growth and tissue formation, but the coordination between Zn^{2+} and PDA on the chelated sites of pyrocatechol (Figure 3G and H) can modulate the bioavailability of the released Zn^{2+} to control the biocompatibility of both Ti-ZnO/PDA and Ti-ZnO/PDA/RGDC. Namely, PDA binds with Zn^{2+} to reduce bioavailability and toxicity of Zn^{2+} (Figure 3G and H), and thus the biocompatibility is enhanced. Therefore, although the amounts of released Zn^{2+} from Ti-ZnO/PDA and Ti-ZnO/PDA/RGDC are larger than that from Ti-ZnO during phosphate-buffered saline (PBS) immersion (Figure 3A1), the cell viability of Ti-ZnO/PDA and Ti-ZnO/PDA/RGDC is much higher than that of Ti-ZnO.

Alkaline Phosphatase (ALP) Activity. Figure 6C presents the specific ALP activities of Ti, Ti-ZnOs, Ti-ZnO, Ti-ZnO/PDA, and Ti-ZnO/PDA/RGDC after 3, 7, and 14 days. Throughout incubation (3, 7, and 14 days), Ti-ZnO exhibits the lowest ALP activity. After coating with PDA and covalent immobilization of the RGDC peptide, the ALP activity increases gradually, and the maximum specific ALP activity of Ti-ZnO/PDA/RGDC is observed on day 14 (75.0 ± 12.0 U/g protein). In general, the ALP activities of all the samples increase gradually with time, and Ti-ZnO/PDA/RGDC shows excellent osteogenic differentiation and improved cell adhesion and proliferation. Zn-implanted biomaterials can regulate initial cell adhesion, spreading, proliferation, and osteogenic differentiation to promote new bone formation *in vitro* and *in vivo*.[14−22] With respect to the hybrid NRs described here, the appropriate concentration of released Zn^{2+} enhances osteogenic differentiation for over 90 days without showing initial burst release (Figure 3A), and PDA can bind with Zn^{2+} (Figure 3G and H). Meanwhile, RGDC is effective in promoting cell attachment and integration with surrounding tissues to facilitate cell attachment.[39]

DOI: 10.1021/acsnano.7b05620
ACS Nano 2017, 11, 11250−11263

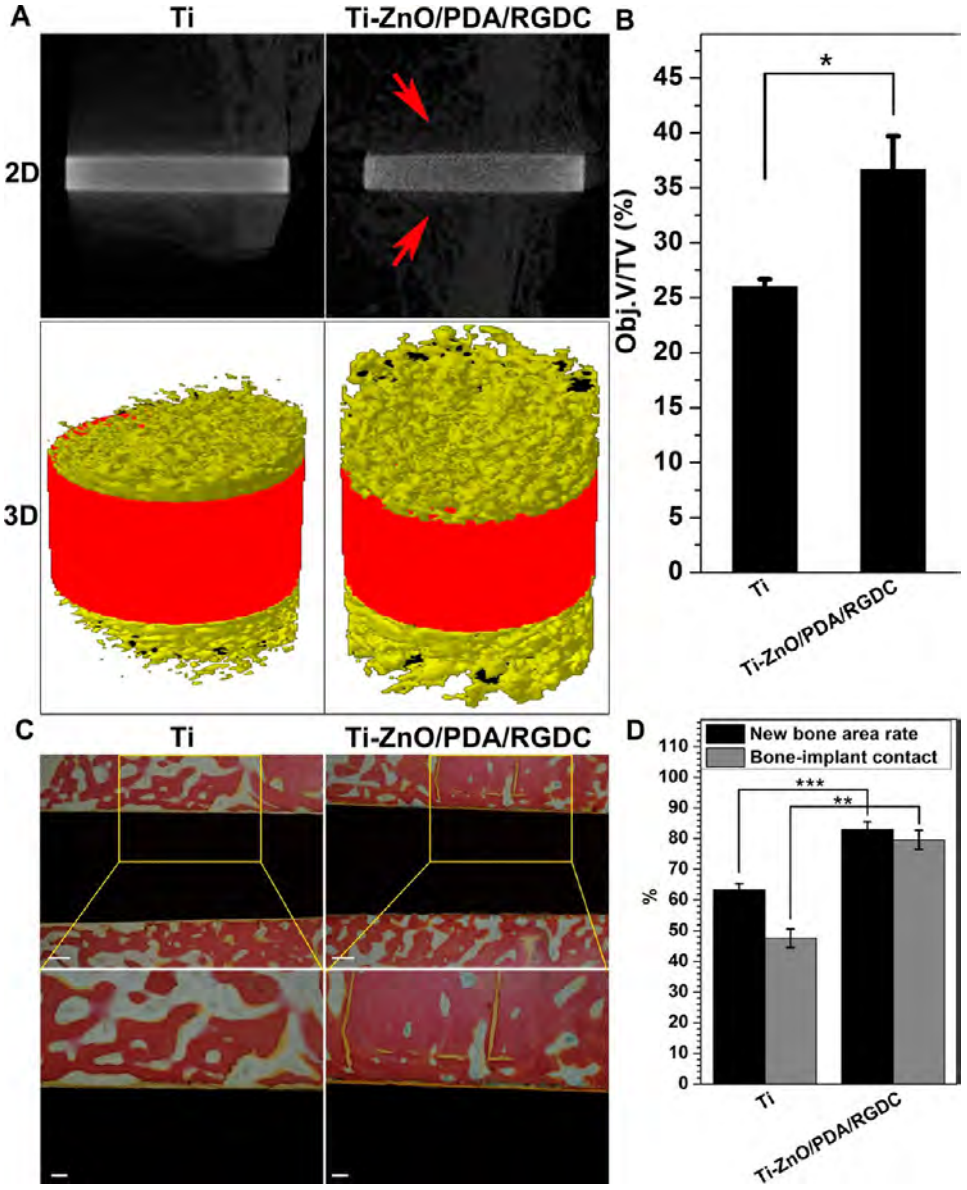

Figure 8. (A) Micro-CT 2D and 3D images of new bone formation around the Ti and Ti-ZnO/PDA/RGDC implants in the rabbit femur 4 weeks after implantation; (B) quantitative measurement of micro-CT 3D images of bone remodeling; (C) histological characteristics at the bone−implant interfaces stained with Van Gieson's picro fuchsin (scale bars = 200 and 100 μm); (D) new bone area rate and bone−implant contact from the histomorphometric measurements. The error bars indicate means ± standard deviations: *P < 0.05, **P < 0.05, and ***P < 0.001 (t test).

Matrix Mineralization and Osteogenesis-Related Gene Expression. To further analyze osteogenic differentiation, the extent of extracellular matrix (ECM) mineralization is evaluated after 7 and 14 days in osteogenic medium extracts (Figure S10). The highest level of mineralization is observed from Ti-ZnO/PDA/RGDC, followed by Ti and Ti-ZnO/PDA. Quantitative measurement of mineralization confirms the results (Figure 6D). The real-time quantitative polymerase chain reaction (RT-QPCR) analysis on the seventh and 14th day (Figure 6E to G) show that Ti-ZnO/PDA/RGDC promotes the expression of ALP (marker of osteoblast differentiation), RUNX2 (master transcription factor for osteoblast differentiation), and OCN (later marker of osteoblastic differentiation) compared to pure Ti. Ti-ZnO exhibits lower gene expressions of ALP, RUNX2, and OCN. Zn-implanted biomaterials can significantly regulate osteogenic differentiation and promote new bone formation by enhancing the gene expressions of ALP, RUNX2, and OCN.[20−22] The results verify further that Ti-ZnO/PDA/RGDC enhances osteogenic differentiation compared to Ti.

***In Vivo* Rabbit Femur Implantation Model.** According to the above results of antibacterial activity and outstanding osteogenic properties *in vitro*, Ti-ZnO/PDA/RGDC is selected for the *in vivo* study. The Ti-based implants are inserted into the femur of adult male New Zealand white rabbits (Figure S11A, black arrow) accompanied by injection of *S. aureus* to simulate implant-associated infection. The X-ray image (Figure S11B, black arrow) and photograph (Figure S11C, black arrow) show the implant position after 4 weeks.

***In Vivo* Antibacterial Ability.** The tissues surrounding the implants are susceptible to exogenous infection during perioperation.[64] A large number of neutrophils in the soft

DOI: 10.1021/acsnano.7b05620
ACS Nano 2017, 11, 11250−11263

tissue and bone reflects bacterial infection because neutrophils migrate rapidly from circulating blood to infected sites in response to infection.[64] Many lobulated neutrophils of hematoxylin and eosin (H&E) staining (red arrow in Figure 7) can be observed from the soft tissue and bone surrounding the implants of the pure Ti group, indicating severe bacterial infection. In comparison, the number of neutrophils of Ti-ZnO/PDA/RGDC is less than that of pure Ti, and the majority of the cells are normal (Figure 7), suggesting relatively minor infection and effective antibacterial ability of Ti-ZnO/PDA/RGDC *in vivo*. The amounts of adherent bacteria in the soft tissues and bone around the implants are observed by Giemsa staining (black arrow in Figure 7). Compared to pure Ti, the amount of bacteria of Ti-ZnO/PDA/RGDC decreases significantly to verify the antibacterial ability of Ti-ZnO/PDA/RGDC *in vivo*. In conclusion, the *in vivo* antibacterial assay is in good agreement with *in vitro* antibacterial evaluation (Figure 4).

Micro-CT Evaluation of Bone Formation. The newly formed bone is monitored by microcomputed tomography (CT) and histopathological evaluation after 4 weeks. Because metal CT artifacts may obscure or simulate pathology, three different cylindrical areas 1.5 mm in diameter and 1 mm thick on both side of the implant surfaces in contact with cancellous bone are chosen as the volume of interest and quantitatively analyzed (Figure 8B) in order to lower the radiation dose and reduce errors.[65] The 2D and 3D images reconstructed by micro-CT of the newly formed bone on the Ti and Ti-ZnO/PDA/RGDC implants are presented in Figure 8A. The red arrow in the 2D image and yellow color in the 3D image mark new bone formation. Ti-ZnO/PDA/RGDC shows significantly more newly formed bone tissues (Obj.V (object volume)/TV (tissue volume) = 36.64 ± 3.07%) than Ti (Obj.V/TV = 25.96 ± 0.72%), as shown in Figure 8B.

Histopathological Evaluation. The bone–implant interfaces of the histological sections are examined by Van Gieson's picro fuchsin staining to study osseointegration through the mineralized bone tissue (red in color) for bone histology. After 4 weeks, a larger newly formed bone area (red in color) and bone–implant contact can be observed from Ti-ZnO/PDA/RGDC (83.5% and 79.6%, respectively) compared to Ti (63.4% and 47.6%, respectively) (Figure 8C and D), indicating that Ti-ZnO/PDA/RGDC enhances the bone density and bone contact to promote rapid osseointegration in the early stage. Zn-implanted biomaterials have been found to have superior bone integration in direct contact form and can accelerate osseointegration.[19−21] Consequently, osteogenesis and osseointegration at the bone–implant interfaces are accelerated because Zn^{2+} release from the hybrid NR arrays is continuous and steady for up to 90 days and plays a crucial role in the osteogenic properties *in vivo* (Figure 3A).

***In Vivo* Toxicology.** The *in vivo* toxicology was examined by the corresponding histological analyses of major organs including the liver, spleen, kidney, heart, and lung by H&E staining and serum aspartate transaminase (AST) and alanine aminotransferase (ALT) related to live enzyme after 2 weeks. In Figure S13A, no significant differences in the control (no treatment), Ti, and Ti-ZnO/PDA/RGDC can be found. Meanwhile, no sign of organ damage can be observed, suggesting no apparent histological toxicology. In addition, the levels of serum AST and ALT related to live enzyme are within the normal ranges of New Zealand white rabbits.[66,67]

From the above results, the bone implant of Ti-ZnO/PDA/RGDC fulfills the following criteria: (a) biocompatibility to induce cell attachment, differentiation, and proliferation; (b) osteoconduction and osteoinduction; (c) biodegradability of modified coatings at an appropriate rate; (d) self-antibacterial ability to inhibit the growth of pathogens. However, antibacterial ability and osteogenic differentiation are hard to achieve together in many strategies of implant surface modification.[68,69] Therefore, balancing the bacteria–osteoblast competition through selective physical puncture and the biofunctionalization of ZnO/PDA/RGDC nanorods can allow sufficient osteoblast growth while inhibiting bacteria, which is more appropriate for implant surface modification.

CONCLUSION

A simple and effective way to fabricate hybrid ZnO/PDA/RGDC NRs is described, and the related mechanism is systematically illustrated in the bacteria–osteoblast "race" through selective physical puncture and the biofunctionalization of ZnO/PDA/RGDC nanorods. The cooperation of selective physical puncture and zinc ions of the hybrid NRs results in effective antibacterial activity as well as excellent osteoinductivity because PDA can bind with Zn^{2+} to promote cytocompatibility and has a strong antioxidant effect to scavenge significantly ROS to minimize possible cytotoxicity. The *in vitro* and *in vivo* results reveal that the hybrid NRs possess contact-killing antibacterial activity against adherent *S. aureus* and *E. coli* as well as outstanding osteogenic properties to enhance the formation of new bone tissues. This platform is widely applied for not only medical implants but also medical devices or medical facilities, such as heart valves, artificial knees, catheters, and vascular grafts to prevent colonization of bacteria on surfaces. The design of 1D hybrid NRs involved in antibacterial therapy, osteointegration, and tissue engineering will bring more insight and understanding to multidisciplinary applications.

ASSOCIATED CONTENT

Supporting Information

The Supporting Information is available free of charge on the ACS Publications website at DOI: 10.1021/acsnano.7b05620.

Additional information (PDF)

AUTHOR INFORMATION

Corresponding Author

*E-mail: shuilin.wu@gmail.com; shuilinwu@tju.edu.cn (S.-L. Wu).

ORCID

Shuilin Wu: 0000-0002-1270-1870

Author Contributions

#J. Li and L. Tan contributed equally to this work and share the co-first authorship.

Notes

The authors declare no competing financial interest.

ACKNOWLEDGMENTS

This work is jointly supported by the National Natural Science Foundation of China, Nos. 51422102 and 81271715, National Key Research and Development Program of China No. 2016YFC1100600 (subproject 2016YFC1100604), Hong Kong Research Grants Council (RGC) General Research

DOI: 10.1021/acsnano.7b05620
ACS Nano 2017, 11, 11250–11263

Funds (GRF) No. 11301215, and City University of Hong Kong Applied Research Grant (ARG) No. 9667144.

REFERENCES

(1) Geetha, M.; Singh, A. K.; Asokamani, R.; Gogia, A. K. Ti Based Biomaterials, the Ultimate Choice for Orthopaedic Implants - A Review. *Prog. Mater. Sci.* **2009**, *54*, 397−425.
(2) Mishnaevsky, L.; Levashov, E.; Valiev, R. Z.; Segurado, J.; Sabirov, I.; Enikeev, N.; Prokoshkin, S.; Solov'yov, A. V.; Korotitskiy, A.; Gutmanas, E.; Gotman, I.; Rabkin, E.; Psakh'e, S.; Dluhoš, L.; Seefeldt, M.; Smolin, A. Nanostructured Titanium-Based Materials for Medical Implants: Modeling and Development. *Mater. Sci. Eng., R* **2014**, *81*, 1−19.
(3) Zhao, Z.; Yan, R.; Yi, X.; Li, J.; Rao, J.; Guo, Z.; Yang, Y.; Li, W.; Li, Y. Q.; Chen, C. Bacteria-Activated Theranostic Nanoprobes against Methicillin-Resistant *Staphylococcus aureus* Infection. *ACS Nano* **2017**, *11*, 4428−4438.
(4) Li, P.; Poon, Y. F.; Li, W.; Zhu, H. Y.; Yeap, S. H.; Cao, Y.; Qi, X.; Zhou, C.; Lamrani, M.; Beuerman, R. W.; Kang, E. T.; Mu, Y.; Li, C. M.; Chang, M. W.; Leong, S. S. J.; Chan-Park, M. B. A Polycationic Antimicrobial and Biocompatible Hydrogel with Microbe Membrane Suctioning Ability. *Nat. Mater.* **2011**, *10*, 149−156.
(5) Neoh, K. G.; Hu, X.; Zheng, D.; Kang, E. T. Balancing Osteoblast Functions and Bacterial Adhesion on Functionalized Titanium Surfaces. *Biomaterials* **2012**, *33*, 2813−2822.
(6) Busscher, H. J.; Van Der Mei, H. C.; Subbiahdoss, G.; Jutte, P. C.; Van Den Dungen, J. J. A. M.; Zaat, S. A. J.; Schultz, M. J.; Grainger, D. W. Biomaterial-Associated Infection: Locating the Finish Line in the Race for the Surface. *Sci. Transl. Med.* **2012**, *4*, 153−163.
(7) Van Oosten, M.; Schäfer, T.; Gazendam, J. A. C.; Ohlsen, K.; Tsompanidou, E.; De Goffau, M. C.; Harmsen, H. J. M.; Crane, L. M. A.; Lim, E.; Francis, K. P.; Cheung, L.; Olive, M.; Ntziachristos, V.; Van Dijl, J. M.; Van Dam, G. M. Real-Time *in Vivo* Imaging of Invasive- and Biomaterial-Associated Bacterial Infections Using Fluorescently Labelled Vancomycin. *Nat. Commun.* **2013**, *4*, 2584−2591.
(8) Zhou, T.; Zhu, Y.; Li, X.; Liu, X.; Yeung, K. W. K.; Wu, S.; Wang, X.; Cui, Z.; Yang, X.; Chu, P. K. Surface Functionalization of Biomaterials by Radical Polymerization. *Prog. Mater. Sci.* **2016**, *83*, 191−235.
(9) Min, J.; Choi, K. Y.; Dreaden, E. C.; Padera, R. F.; Braatz, R. D.; Spector, M.; Hammond, P. T. Designer Dual Therapy Nanolayered Implant Coatings Eradicate Biofilms and Accelerate Bone Tissue Repair. *ACS Nano* **2016**, *10*, 4441−4450.
(10) Xie, X.; Mao, C.; Liu, X.; Zhang, Y.; Cui, Z.; Yang, X.; Yeung, K. W. K.; Pan, H.; Chu, P. K.; Wu, S. Synergistic Bacteria Killing through Photodynamic and Physical Actions of Graphene Oxide/Ag/Collagen Coating. *ACS Appl. Mater. Interfaces* **2017**, *9*, 26417−26428.
(11) Pan, G.; Sun, S.; Zhang, W.; Zhao, R.; Cui, W.; He, F.; Huang, L.; Lee, S. H.; Shea, K. J.; Shi, Q.; Yang, H. Biomimetic Design of Mussel-Derived Bioactive Peptides for Dual-Functionalization of Titanium-Based Biomaterials. *J. Am. Chem. Soc.* **2016**, *138*, 15078−15086.
(12) Perez, R. A.; Choi, S. J.; Han, C. M.; Kim, J. J.; Shim, H.; Leong, K. W.; Kim, H. W. Biomaterials Control of Pluripotent Stem Cell Fate for Regenerative Therapy. *Prog. Mater. Sci.* **2016**, *82*, 234−293.
(13) Ivanova, E. P.; Hasan, J.; Webb, H. K.; Gervinskas, G.; Juodkazis, S.; Truong, V. K.; Wu, A. H. F.; Lamb, R. N.; Baulin, V. A.; Watson, G. S.; Watson, J. A.; Mainwaring, D. E.; Crawford, R. J. Bactericidal Activity of Black Silicon. *Nat. Commun.* **2013**, *4*, 2838−2844.
(14) Park, J. K.; Kim, Y. J.; Yeom, J.; Jeon, J. H.; Yi, G. C.; Je, J. H.; Hahn, S. K. The Topographic Effect of Zinc Oxide Nanoflowers on Osteoblast Growth and Osseointegration. *Adv. Mater.* **2010**, *22*, 4857−4851.
(15) Wang, Z. L. ZnO Nanowire and Nanobelt Platform for Nanotechnology. *Mater. Sci. Eng., R* **2009**, *64*, 33−71.
(16) Wang, T.; Liu, X.; Zhu, Y.; Cui, Z. D.; Yang, X. J.; Pan, H.; Yeung, K. W. K.; Wu, S. Metal Ion Coordination Polymer-Capped pH-Triggered Drug Release System on Titania Nanotubes for Enhancing Self-antibacterial Capability of Ti Implants. *ACS Biomater. Sci. Eng.* **2017**, *3*, 816−825.
(17) Zhou, J.; Xu, N. S.; Wang, Z. L. Dissolving Behavior and Stability of ZnO Wires in Biofluids: A Study on Biodegradability and Biocompatibility of ZnO Nanostructures. *Adv. Mater.* **2010**, *18*, 2432−2435.
(18) Jin, G.; Cao, H.; Qiao, Y.; Meng, F.; Zhu, H.; Liu, X. Osteogenic Activity and Antibacterial Effect of Zinc Ion Implanted Titanium. *Colloids Surf., B* **2014**, *117*, 158−165.
(19) Huo, K.; Zhang, X.; Wang, H.; Zhao, L.; Liu, X.; Chu, P. K. Osteogenic Activity and Antibacterial Effects on Titanium Surfaces Modified with Zn-Incorporated Nanotube Arrays. *Biomaterials* **2013**, *34*, 3467−3478.
(20) Jin, G.; Qin, H.; Cao, H.; Qian, S.; Zhao, Y.; Peng, X.; Zhang, X.; Liu, X.; Chu, P. K. Synergistic Effects of Dual Zn/Ag Ion Implantation in Osteogenic Activity and Antibacterial Ability of Titanium. *Biomaterials* **2014**, *35*, 7699−7713.
(21) Qiao, Y.; Zhang, W.; Tian, P.; Meng, F.; Zhu, H.; Jiang, X.; Liu, X.; Chu, P. K. Stimulation of Bone Growth Following Zinc Incorporation into Biomaterials. *Biomaterials* **2014**, *35*, 6882−6897.
(22) Shen, X.; Hu, Y.; Xu, G.; Chen, W.; Xu, K.; Ran, Q.; Ma, P.; Zhang, Y.; Li, J.; Cai, K. Regulation of the Biological Functions of Osteoblasts and Bone Formation by Zn-Incorporated Coating on Microrough Titanium. *ACS Appl. Mater. Interfaces* **2014**, *6*, 16426−16440.
(23) Zhu, P.; Weng, Z.; Li, X.; Liu, X.; Wu, S.; Yeung, K. W. K.; Wang, X.; Cui, Z.; Yang, X.; Chu, P. K. Biomedical Applications of Functionalized ZnO Nanomaterials: from Biosensors to Bioimaging. *Adv. Mater. Interfaces* **2016**, *3*, 1500494.
(24) Noimark, S.; Weiner, J.; Noor, N.; Allan, E.; Williams, C. K.; Shaffer, M. S. P.; Parkin, I. P. Dual-Mechanism Antimicrobial Polymer−ZnO Nanoparticle and Crystal Violet-Encapsulated Silicone. *Adv. Funct. Mater.* **2015**, *25*, 1367−1373.
(25) Zhong, Z.; Xu, Z.; Sheng, T.; Yao, J.; Xing, W.; Wang, Y. Unusual Air Filters with Ultrahigh Efficiency and Antibacterial Functionality Enabled by ZnO Nanorods. *ACS Appl. Mater. Interfaces* **2015**, *7*, 21538−21544.
(26) Li, Y.; Zhang, W.; Niu, J.; Chen, Y. Mechanism of Photogenerated Reactive Oxygen Species and Correlation with the Antibacterial Properties of Engineered Metal-Oxide Nanoparticles. *ACS Nano* **2012**, *6*, 5164−5173.
(27) Cha, S. H.; Hong, J.; McGuffie, M.; Yeom, B.; VanEpps, J. S.; Kotov, N. A. Shape-Dependent Biomimetic Inhibition of Enzyme by Nanoparticles and Their Antibacterial Activity. *ACS Nano* **2015**, *9*, 9097−9105.
(28) Schwartz, V. B.; Thétiot, F.; Ritz, S.; Pütz, S.; Choritz, L.; Lappas, A.; Förch, R.; Landfester, K.; Jonas, U. Antibacterial Surface Coatings from Zinc Oxide Nanoparticles Embedded in Poly(N-isopropylacrylamide) Hydrogel Surface Layers. *Adv. Funct. Mater.* **2012**, *22*, 2376−2386.
(29) Lee, J.; Kang, B. S.; Hicks, B.; Chancellor, C. T.; Chu, B. H.; Wang, H. T.; Keselowsky, B. G.; Ren, F.; Lele, T. P. The Control of Cell Adhesion and Viability by Zinc Oxide Nanorods. *Biomaterials* **2008**, *29*, 3743−3749.
(30) Zaveri, T. D.; Dolgova, N. V.; Chu, B. H.; Lee, J.; Wong, J.; Lele, T. P.; Ren, F.; Keselowsky, B. G. Contributions of Surface Topography and Cytotoxicity to the Macrophage Response to Zinc Oxide Nanorods. *Biomaterials* **2010**, *31*, 2999−3007.
(31) Müller, K. H.; Kulkarni, J.; Motskin, M.; Goode, A.; Winship, P.; Skepper, J. N.; Ryan, M. P.; Porter, A. E. pH-Dependent Toxicity of High Aspect Ratio ZnO Nanowires in Macrophages Due to Intracellular Dissolution. *ACS Nano* **2010**, *4*, 6767−6779.
(32) Petrochenko, P. E.; Zhang, Q.; Bayati, R.; Skoog, S. A.; Phillips, K. S.; Kumar, G.; Narayan, R. J.; Goering, P. L. Cytotoxic Evaluation of Nanostructured Zinc Oxide (ZnO) Thin Films and Leachates. *Toxicol. In Vitro* **2014**, *28*, 1144−1152.

DOI: 10.1021/acsnano.7b05620
ACS Nano 2017, 11, 11250−11263

(33) Song, W.; Zhang, J.; Guo, J.; Zhang, J.; Ding, F.; Li, L.; Sun, Z. Role of the Dissolved Zinc Ion and Reactive Oxygen Species in Cytotoxicity of ZnO Nanoparticles. *Toxicol. Lett.* **2010**, *199*, 389−397.
(34) James, S. A.; Feltis, B. N.; de Jonge, M. D.; Sridhar, M.; Kimpton, J. A.; Altissimo, M.; Mayo, S.; Zheng, C.; Hastings, A.; Howard, D. L.; Paterson, D. J.; Wright, P. F. A.; Moorhead, G. F.; Turney, T. W.; Fu, J. Quantification of ZnO Nanoparticle Uptake, Distribution, and Dissolution within Individual Human Macrophages. *ACS Nano* **2013**, *7*, 10621−10635.
(35) Applerot, G.; Lipovsky, A.; Dror, R.; Perkas, N.; Nitzan, Y.; Lubart, R.; Gedanken, A. Enhanced Antibacterial Activity of Nanocrystalline ZnO Due to Increased ROS-Mediated Cell Injury. *Adv. Funct. Mater.* **2009**, *19*, 842−852.
(36) He, W.; Kim, H. K.; Wamer, W. G.; Melka, D.; Callahan, J. H.; Yin, J. J. Photogenerated Charge Carriers and Reactive Oxygen Species in ZnO/Au Hybrid Nanostructures with Enhanced Photocatalytic and Antibacterial Activity. *J. Am. Chem. Soc.* **2014**, *136*, 750−757.
(37) Lee, H.; Dellatore, S. M.; Miller, W. M.; Messersmith, P. B. Mussel-Inspired Surface Chemistry for Multifunctional Coatings. *Science* **2007**, *318*, 426−430.
(38) Liu, Y.; Ai, K.; Lu, L. Polydopamine and Its Derivative Materials: Synthesis and Promising Applications in Energy, Environmental, and Biomedical Fields. *Chem. Rev.* **2014**, *114*, 5057−5115.
(39) Bellis, S. L. Advantages of RGD Peptides for Directing Cell Association with Biomaterials. *Biomaterials* **2011**, *32*, 4205−4210.
(40) Wong, D. S. H.; Li, J.; Yan, X.; Wang, B.; Li, R.; Zhang, L.; Bian, L. Magnetically Tuning Tether Mobility of Integrin Ligand Regulates Adhesion, Spreading, and Differentiation of Stem Cells. *Nano Lett.* **2017**, *17*, 1685−1695.
(41) Rouabhia, M.; Asselin, J.; Tazi, N.; Messaddeq, Y.; Levinson, D.; Zhang, Z. Production of Biocompatible and Antimicrobial Bacterial Cellulose Polymers Functionalized by RGDC Grafting Groups and Gentamicin. *ACS Appl. Mater. Interfaces* **2014**, *6*, 1439−1446.
(42) Nguyen, M. N.; Lebarbe, T.; Zouani, O. F.; Pichavant, L.; Durrieu, M. C.; Héroguez, V. Impact of RGD Nanopatterns Grafted onto Titanium on Osteoblastic Cell Adhesion. *Biomacromolecules* **2012**, *13*, 896−904.
(43) Stevens, M. M.; George, J. H. Exploring and Engineering the Cell Surface Interface. *Science* **2005**, *310*, 1135−1138.
(44) Phuruangrat, A.; Dumrongrojthanath, P.; Yayapao, O.; Arin, J.; Thongtem, S.; Thongtem, T. Photocatalytic Activity of La-Doped ZnO Nanostructure Materials Synthesized by Sonochemical Method. *Rare Met.* **2016**, *35*, 390−395.
(45) Wang, L.; Liu, S.; Feng, X.; Xu, Q.; Bai, S.; Zhu, L.; Chen, L.; Qin, Y.; Wang, Z. L. Ultrasensitive Vertical Piezotronic Transistor Based on ZnO Twin Nanoplatelet. *ACS Nano* **2017**, *11*, 4859−4865.
(46) Esro, M.; Vourlias, G.; Somerton, C.; Milne, W. I.; Adamopoulos, G. High-Mobility ZnO Thin Film Transistors Based on Solution-Processed Hafnium Oxide Gate Dielectrics. *Adv. Funct. Mater.* **2015**, *25*, 134−141.
(47) Hagendorfer, H.; Lienau, K.; Nishiwaki, S.; Fella, C. M.; Kranz, L.; Uhl, A. R.; Jaeger, D.; Luo, L.; Gretener, C.; Buecheler, S.; Romanyuk, Y. E.; Tiwan, A. N. Highly Transparent and Conductive ZnO: Al Thin Films from a Low Temperature Aqueous Solution Approach. *Adv. Mater.* **2014**, *26*, 632−636.
(48) Yuan, N. Y.; Wang, S. Y.; Tan, C. B.; Wang, X. Q.; Chen, G. G.; Ding, J. N. The Influence of Deposition Temperature on Growth Mode, Optical and Mechanical Properties of ZnO Films Prepared by the ALD Method. *J. Cryst. Growth* **2013**, *366*, 43−46.
(49) Luo, R.; Tang, L.; Zhong, S.; Yang, Z.; Wang, J.; Weng, Y.; Tu, Q.; Jiang, C.; Huang, N. *In Vitro* Investigation of Enhanced Hemocompatibility and Endothelial Cell Proliferation Associated with Quinone-Rich Polydopamine Coating. *ACS Appl. Mater. Interfaces* **2016**, *5*, 1704−1714.
(50) Zheng, W.; Fan, H.; Wang, L.; Jin, Z. Oxidative Self-Polymerization of Dopamine in Acidic Environment. *Langmuir* **2015**, *31*, 11671−11677.
(51) Iqbal, Z.; Lai, E. P. C.; Avis, T. J. Antimicrobial Effect of Polydopamine Coating on *Escherichia coli*. *J. Mater. Chem.* **2012**, *22*, 21608−21612.
(52) Hersel, U.; Dahmen, C.; Kessler, H. RGD Modified Polymers: Biomaterials for Stimulated Cell Adhesion and Beyond. *Biomaterials* **2003**, *24*, 4385−4415.
(53) Desseaux, S.; Klok, H. A. Fibroblast Adhesion on ECM-Derived Peptide Modified Poly(2-hydroxyethyl methacrylate) Brushes: Ligand Co-Presentation and 3D-Localization. *Biomaterials* **2015**, *44*, 24−35.
(54) Xu, L. Q.; Yang, W. J.; Neoh, K. G.; Kang, E. T.; Fu, G. D. Dopamine-Induced Reduction and Functionalization of Graphene Oxide Nanosheets. *Macromolecules* **2010**, *43*, 8336−8339.
(55) Lee, H.; Rho, J.; Messersmith, P. B. Facile Conjugation of Biomolecules onto Surfaces *via* Mussel Adhesive Protein Inspired Coatings. *Adv. Mater.* **2009**, *21*, 431−434.
(56) Feng, X.; Feng, L.; Jin, M.; Zhai, J.; Jiang, L.; Zhu, D. Reversible Super-Hydrophobicity to Super-Hydrophilicity Transition of Aligned ZnO Nanorod Films. *J. Am. Chem. Soc.* **2004**, *126*, 62−63.
(57) Liao, H.; Andersson, A. S.; Sutherland, D.; Petronis, S.; Kasemo, B.; Thomsen, P. Response of Rat Osteoblast-like Cells to Micro-structured Model Surfaces. *Biomaterials* **2003**, *24*, 649−654.
(58) Wu, S.; Liu, X.; Hu, T.; Chu, P. K.; Ho, J. P. Y; Chan, Y. L.; Yeung, K. W. K; Chu, C. L.; Hung, T. F.; Huo, K. F.; Chung, C. Y.; Lu, W. W.; Cheung, K. M. C.; Luk, K. D. K. A Biomimetic Hierarchical Scaffold: Natural Growth of Nanotitanates on Three-Dimensional Microporous Ti-Based Metals. *Nano Lett.* **2008**, *8*, 3803−3808.
(59) Pezzella, A.; D'Ischia, M.; Napolitano, A.; Palumbo, A.; Prota, G. An Integrated Approach to the Structure of Sepia Melanin. Evidence for a High Proportion of Degraded 5,6-dihydroxyindole-2-carboxylic Acid Units in the Pigment Backbone. *Tetrahedron* **1997**, *53*, 8281−8286.
(60) Liu, Y.; Ai, K.; Liu, J.; Deng, M.; He, Y.; Lu, L. Dopamine-Melanin Colloidal Nanospheres: An Efficient Near-Infrared Photothermal Therapeutic Agent for *In Vivo* Cancer Therapy. *Adv. Mater.* **2013**, *25*, 1353−1359.
(61) Fu, P. P.; Xia, Q.; Hwang, H. M.; Ray, P. C.; Yu, H. Mechanisms of Nanotoxicity: Generation of Reactive Oxygen Species. *J. Food Drug Anal.* **2014**, *22*, 64−75.
(62) Wei, Y.; Guo, M. Zinc-Binding Sites on Selected Flavonoids. *Biol. Trace Elem. Res.* **2014**, *161*, 223−230.
(63) Xia, D.; Shen, Z.; Huang, G.; Wang, W.; Yu, J. C.; Wong, P. K. Red phosphorus: An Earth-Abundant Elemental Photocatalyst for "Green" Bacterial Inactivation under Visible Light. *Environ. Sci. Technol.* **2015**, *49*, 6264−6273.
(64) Wang, J.; Li, J.; Qian, S.; Guo, G.; Wang, Q.; Tang, J.; Shen, H.; Liu, X.; Zhang, X.; Chu, P. K. Antibacterial Surface Design of Titanium-Based Biomaterials for Enhanced Bacteria-Killing and Cell-Assisting Functions Against Periprosthetic Joint Infection. *ACS Appl. Mater. Interfaces* **2016**, *8*, 11162−11178.
(65) Boas, F. E.; Fleischmann, D. CT Artifacts: Causes and Reduction Techniques. *Imaging Med.* **2016**, *4*, 229−240.
(66) Yildiz-Gulay, O.; Gulay, M. S.; Ata, A.; Balic, A.; Demirtas, A. The Effects of Feeding Pinus Pinea Seeds on Some Blood Values in Male New Zealand White Rabbits. *J. Anim. Vet. Adv.* **2010**, *9*, 2655−2658.
(67) Gulay, M. S.; Yildiz-Gulay, O.; Ata, A.; Balic, A.; Demirtas, A. Toxicological Evaluation of Carob (Ceratonia silique) Bean Extracts in Male New Zealand White Rabbits. *J. Anim. Vet. Adv.* **2012**, *11*, 1853−1857.
(68) Tsimbouri, P. M.; Fisher, L.; Holloway, N.; Sjostrom, T.; Nobbs, A. H.; Meek, R. M. D.; Su, B.; Dalby, M. J. Osteogenic and Bactericidal Surfaces from Hydrothermal Titania Nanowires on Titanium Substrates. *Sci. Rep.* **2016**, *6*, 36857−36868.
(69) Liao, H.; Miao, X.; Ye, J.; Wu, T.; Deng, Z.; Li, C.; Jia, J.; Cheng, X.; Wang, X. Falling Leaves Inspired ZnO Nanorods-Nanoslices Hierarchical Structure for Implant Surface Modification with Two Stage Releasing Features. *ACS Appl. Mater. Interfaces* **2017**, *9*, 13009−13015.

DOI: 10.1021/acsnano.7b05620
ACS Nano 2017, 11, 11250−11263

Supporting Information

Balancing Bacteria-Osteoblasts Competition through Selective Physical Puncture and Biofunctionalization of ZnO/Polydopamine/Arginine-Glycine-Aspartic Acid-Cysteine Nanorods

*Jun Li,[a,#] Lei Tan,[a,#] Xiangmei Liu,[a] Zhenduo Cui,[b] Xianjin Yang,[b] Kelvin Wai Kwok Yeung,[c] Paul K Chu,[d] Shuilin Wu[a,b]**

[a] Hubei Collaborative Innovation Center for Advanced Organic Chemical Materials, Ministry-of-Education Key Laboratory for the Green Preparation and Application of Functional Materials, Hubei Key Laboratory of Polymer Materials, School of Materials Science & Engineering, Hubei University, Wuhan 430062, China

[b] School of Materials Science & Engineering, Tianjin University, Tianjin 300072, China

[c] Department of Orthopaedics & Traumatology, Li Ka Shing Faculty of Medicine, The University of Hong Kong, Pokfulam, Hong Kong, China

[d] Department of Physics & Materials Science, City University of Hong Kong, Tat Chee Avenue, Kowloon, Hong Kong, China

 # The two authors contributed equally to this work and share the co-first authorship

* To whom correspondence should be addressed:

E-mail: shuilin.wu@gmail.com; shuilinwu@tju.edu.cn (S.L. Wu)

Table of contents

1. EXPERIMENTAL SECTION

1.1 Materials

The medical pure Ti was purchased from Baosteel Group Corp, Shanghai China. Zinc nitrate hexahydrate ($Zn(NO_3)_2•6H_2O$), hexamethylenetetramine (HMTA, $C_6H_{12}N_4$), ethanol, and acetone were acquired from Sinopharm Chemical Reagent Co. (China). Dopamine hydrochloride was bought from Aladdin Industrial Co. (China) and RGDC peptide from GL Biochem (Shanghai) Ltd.

1.2 Physical polishing treatment of Ti surface

The medical pure Ti with 6 mm diameter and 2 mm thick was employed as substrates. The substrates were mechanically polished with SiC sandpaper (grain sizes from #240 to #2400) and ultrasonically cleaned for 15 min in acetone, ethanol, and deionized water sequentially to remove contaminants.

1.3 ZnO seed layer deposition by ALD

The ZnO seed layer with a thickness of about 40 nm was deposited on the Ti substrate by atomic layer deposition (ALD, F-100-41, MNT Micro and Nanotech Co., LTD, Wuxi, China) using diethyl zinc (DEZ, $(C_2H_5)_2Zn$) and H_2O as the precursors for zinc and oxygen, respectively. The substrate temperature was maintained at 100 °C during deposition. Each cycle consisted of precursor exposure and N_2 purging following a sequence of H_2O:N_2:DEZ:N_2 with the corresponding duration of 0.1:20:0.1:20 s. The purging gas was at a pressure of 40 Pa. The reaction was repeated 300 cycles to obtain

the ZnO films.

1.4 Hydrothermal growth of ZnO NR arrays

After ALD, the seeded Ti substrates were suspended upside down in a Teflon-lined stainless steel autoclave filled with an equimolar aqueous solution (0.025 M) of $Zn(NO_3)_2 \cdot 6H_2O$ and HMTA at 90 °C for 6 h as described previously.[1,2] After the reaction, the autoclave was cooled down naturally to room temperature and the substrates were washed repeatedly with deionized water and dried in air at room temperature.

1.5 PDA coating

The samples of Ti-ZnO were immersed in 2 mg/mL dopamine hydrochloride in 10 mM Tris-HCl buffer (pH 8.5) for 12 h in darkness at room temperature.[3] The coated surfaces were rinsed with deionized water and dried in air at room temperature..

1.6 Covalent immobilization of RGDC peptide

The samples of Ti-ZnO/PDA were immersed in 2 mg/mL RGDC peptide solution in PBS (pH 7.4) for 12 h at room temperature. The samples of Ti-ZnO/PDA/RGDC were rinsed repeatedly with deionized water and dried in air at room temperature.

1.7 Surface characterization

The surface morphology and cross-section of the samples were observed by FE-SEM

(JSM7100F, JEOL, JP) equipped with energy-dispersive spectroscopy (EDS) and SEM (JEOL-820 and JSM6510LV). A transmission electron microscope (TEM; Tecnai G20, FEI, USA) equipped with selected area electron diffraction (SAED) was employed to examine the microstructure and crystal structure of the ZnO NR. The crystal structure was investigated by XRD (D/MAX-IIIC, Rigaku) using Cu K_{α} radiation (λ = 0.15406 nm) at 40 kV and 30 mA. The diffraction angle (2θ) was ranged from 20° to 80° with a step size of 0.02°. To determine the chemical composition and functional groups in the coatings, FTIR (Nicolet570) was performed in the wave number range of 4000–450 cm^{-1}. The powders were scraped with a blade from the surface of the samples and ground with dehydrated KBr. The mixtures were squeezed in a mold to produce disks for FTIR analysis. The surface elemental composition was determined by XPS (Escalab 250Xi). The water contact angles were measured on a JC2000D contact angle system (POWEREACH, China) at ambient temperature. Deionized water was utilized as the medium and three samples were measured for each group for statistical accountability.

1.8 Zn^{2+} release into PBS

Inductively-coupled plasma atomic emission spectrometry (ICP-AES; Optimal 8000, Perkin Elmer, US) was applied to analyze the release behavior of Zn ion. Three Ti plates of each experimental group were immersed in 5 mL of PBS at 37 °C in darkness for 13 weeks and the entire volume was collected at regular time intervals and 5 mL of fresh PBS were refilled accordingly.

1.9 UV-vis absorption spectrophotometry

Dopamine hydrochloride in 10 mM Tris-HCl buffer (pH 8.5) was reacted with the samples of Ti-ZnO or 1 mM H_2O_2 for 12 h in darkness at room temperature. The UV-vis absorption between 500 nm and 1000 nm was measured on a microplate reader (SpectraMax I3MD USA).

1.10 Nuclear magnetic resonance (NMR)

NMR was performed in D_2O. The sample of Ti-ZnO was immersed in 2 mg/mL dopamine hydrochloride at pH of 8.5 adjusted by $NaHCO_3$ for 12 h in darkness at room temperature and named ZnO/PDA as the experimental group. 2 mg/mL dopamine hydrochloride with a pH of 8.5 adjusted by $NaHCO_3$ was reacted for 12 h in darkness at room temperature and named PDA as the control group. The supernatant was collected and used to the ^{1}HNMR spectra were recorded on a UNITY INVOA 600 MHz spectrometer (Varian, USA).

1.11 Electron spin resonance (ESR)

The electron spin resonance (ESR) spectra were recorded on a JES-FA200 spectrometer. 5,5-Dimethyl-1-pyrroline-N-oxide (DMPO) (Sigma) was used for trapping ·OH. The samples of Ti, Ti-ZnOs, Ti-ZnO, Ti-ZnO/PDA, Ti-ZnO/PDA/RGDC and Ti-ZnOs/PDA/RGDC were immersed in 100 mM DMPO at ambient temperature without light illumination. The measurements were repeated

three times for each sample. The ESR measurement was carried out at a frequency of 8.93 GHz, sweeping time of 30 s, time constant of 0.03 sec, and power of 3 mW.

1.12 Evaluation of antibacterial activity *in vitro*

The *in vitro* antibacterial activity against gram-positive *S. aureus* and gram-negative *E. coli* was assessed by bacteria counting method, Live/Dead staining and FE-SEM. The bacteria were cultured in the standard Luria−Bertani (LB) culture medium. The samples were placed on a 48-well plate and 400 μL of the bacterial suspension (10^7 CFU/mL) were added to each well. The samples were incubated in the medium and placed in an orbital shaker at 200 rpm at 37 °C for 12 h with *E. coli* or *S. aureus*. Ti-ZnOs, Ti-ZnO, Ti-ZnO/PDA, and Ti-ZnO/PDA/RGDC constituted the experimental groups and pure Ti was the control group. Three parallel samples from each group were used in the antibacterial test. In the bacteria counting method, after incubation at 37 °C for 12 h, the samples were collected and in 1 mL of sterile PBS. The bacteria adhered to the Ti disks were dislodged by sonication for 1 minute in an ultrasonic bath operated at 50 Hz. The dissociated bacteria suspension was diluted 10000 times for *S. aureus* and 100 times for *E. coli* with sterile PBS. 20 μL of the diluted bacteria suspension were plated on standard Luriae-Bertani (LB) agar and incubated at 37 °C for another 24 h. The active bacteria were counted according to the National Standard of China GB/T 4789.2 protocol and the antibacterial ratio was calculated by the following formula:

$$\text{Antibacterial ratio (\%)} = \frac{\text{A - B}}{\text{A}} \times 100\%$$

,

where A is the average number of bacteria colonies on the control group (Ti samples, CFU/sample) and B is the average number of bacteria colonies on the experimental samples (CFU/sample).[6,7] Prior to fluorescence observation, the samples were stained with Live/Dead Bacterial Viability Kit. The bacteria on the samples were qualitatively examined by FE-SEM. Briefly, after incubation at 37 °C for 12 h, the samples were collected and immersed in a 2.5% glutaraldehyde solution for 2 h. Afterwards, the samples were rinsed with sterile PBS twice and serially dehydrated using a series of ethanol solutions (30, 50, 70, 90 and 100% v/v) for 15 min sequentially.

The permeability of bacterial membrane was defined following the o-nitrophenyl-β-D-galactosidase (ONPG) assay kit procedure (Cayman Chemical Company, Ann Arbor, MI). The protein concentration of bacteria was investigated by an Enhanced BCA Protein Assay Kit (cat# P0010; Beyotime, Jiangsu, China). The level of bacterial ATP was determined with the firefly luciferase method using an Enhanced ATP Assay Kit (cat# S0027; Beyotime).

S. aureus and *E. coli* were inoculated with Ti-ZnOs/PDA/RGDC and Ti-ZnO/PDA/RGDC at 37 °C for 12 h. The samples were fixed with 2.5% glutaraldehyde for 2 h and postfixed with 1% of osmic acid at 4 °C for 2 h, and washed three times with PBS. The samples were dehydrated through a concentration series of ethanol (50%, 70%, 80%, 90% and 95% for 15 min each, 100% for 15 min twice). Then, the samples were embedded and cut into ultrathin sections between 60

nm and 80 nm, and stained with 2% uranium acetate and lead citrate for 15 min each. After drying, the sections were observed by TEM.

1.13 *In vitro* cytocompatibility evaluation

1.13.1 Cell morphology

The cell morphology was observed by fluorescence microscopy (IFM, Olympus, IX73) and SEM. The samples were placed on a 48-well plate and 400 μL of the cell suspension (5×10^4 cells/cm^2) were added to each well and cultured for 1 day. After incubation for 1 day, the samples were rinsed with sterile PBS three times and fixed in 4% formaldehyde at room temperature for 10 min, followed by rinsing with sterile PBS. They were then stained with FITC (YiSen, Shanghai) for 30 min in the dark environment, rinsed with sterile PBS three times, and further stained with DAPI (YiSen, Shanghai) for 30 s, rinsed with sterile PBS three times. The same SEM procedures described above were adopted to observe bacteria by FE-SEM.

1.13.2 *In vitro* cytotoxicity evaluation

The MTT assay was utilized to determine the cytotoxicity to cells by measuring the osteoblast viability. 5×10^4 cells/cm^2 MC3T3-E1 pre-osteoblasts were cultured in dulbecco's modified eagle medium (DMEM) supplemented with 10% (v/v) fetal bovine serum (FBS), 1% penicillin, and 1% amphotericin at 37 °C in an atmosphere of 5% CO_2 and 95% air. The following five groups of samples were tested: Ti, Ti-ZnOs, Ti-ZnO, Ti-ZnO/PDA, and Ti-ZnO/PDA/RGDC. The medium was changed

every three days. The samples were placed on a 48-well plate and 400 μL of the cell suspension (5×10^4 cells/cm^2) were added to each well. After incubation for different time periods (1 day, 3 days and 7 days), 0.5 mg/mL MTT (Aladdin Reagent Co., China) was added. After incubating with MTT for 4 h, the MTT solution was removed and 200 μL of DMSO were added to dissolve the crystals under vibration for 10 min. Finally, the absorption at 570 nm was measured on a microplate reader (SpectraMax I3MD USA) and the cell viability in comparison to the control was determined from the absorbance readings. The cell viability (%) was calculated by comparing the absorbance values of the samples with that of the control.

1.13.3 ALP activity

The ALP assay was performed to determine the osteogenic differentiation properties. Similar to the MTT assay, the samples were placed on a 48-well plate and 400 μL of the cell suspension (5×10^4 cells/cm^2) were added to each well. The culture medium was cultured for 3, 7 or 14 days and changed every 3 days. After incubation, the cells were lysed in 1% Triton X-100 dissolved in PBS and stored in 37 ℃ for 60 min. The intracellular ALP activity was determined by ALP detection kit.

1.13.4 Matrix mineralization and osteogenesis-related gene expression

The extent of the matrix mineralization was determined by Alizarin Red staining. Five samples were placed in the cell cultures and then changed to the osteogenic extracts medium (10^{-8} M dexamethasone, 10 mM β-glycerol phosphate, and 50 μg/mL

ascorbic acid) after incubation for 24 h.[8] The medium was changed every 3 days. After 7 and 14 days, the cells were rinsed with PBS 3 times and fixed in 75% ethanol for 1 h. The fixed cells were stained with 5.55 mM Alizarin Red (pH = 4.2) at room temperature for 10 min and rinsed in distilled water 3 times. The calcium nodule staining was photographed on the Nikon ts100. To conduct the quantitative analysis, the mineralized nodules were dissolved by 10% hexadecylpyridinium chloride and the OD values of absorbance were obtained at 562 nm. Similarly，after the cells were cultured for 7 and 14 days on the various samples (20 mm in diameter and 2 mm long) on 12-well plates, the cellular total RNA was isolated using the Total RNA Kit (OMEGA) and reversely transcripted to cDNA with a PrimeScript RT Master Mix (TaKaRa, Japan) according to the manufacturer's protocols. RT-PCR was performed on a Bio-Rad real-time PCR system. The gene expression of ALP, RUNX2, and OCN was analyzed and the gene expression level of β-actin was used as normalization. The specific forward and reverse primer sequences of the above-mentioned genes are listed in Table S2. Quantification of the gene expressions was based on the comparative cycle-threshold method.

1.14 *In vivo* biological evaluation

1.14.1 Surgical implantation of *in vivo* animal study

All the animal experiments and procedures were approved by the Department of Orthopedic Surgery, Union Hospital, Tongji Medical College, Huazhong University of Science and Technology, Wuhan 430022, People's Republic of China. Ten adult male

New Zealand white rabbits weighing between 2.5 and 3 kg were used. The rabbits were divided into two groups of 5 as follows: Ti and Ti-ZnO/PDA/RGDC. The rabbits were anaesthetized with 3% pentobarbital (1 mL/kg) prior to surgery and placed on a sterile drape to provide sterile conditions during surgery. The site of operation was the right femur and the right leg was shaved, depilated, and disinfected with povidone iodine. To expose the right femur, a medial skin incision was made and a hole perpendicular to the long axis of the femur was drilled to access the medullary cavity. Afterwards, 20 μL of the bacterial suspension with a density of 10^5 CFU/mL *S. aureus* were injected into the implants (6 mm in diameter and 1 mm long) and then the implants were knocked into the holes. The soft tissue and skin were sutured carefully. After the surgery, the rabbits were housed in separate cages and fed in the same way.

1.14.2 Sample preparation

Two rabbits from each group were sacrificed after 2 weeks for histological evaluation to evaluate bacterial infection of the soft tissue and bone around the implants by H&E and Giemsa staining. In addition, *in vivo* toxicology of heart, liver, spleen, lung, and kidney was examined by H&E staining and the levels of serum AST and ALT related to live enzyme were investigated after 2 weeks. The remaining three rabbits from each group were sacrificed after 4 weeks and the right femurs with the implants were examined by X-ray, micro-CT analysis, and histological analysis.

1.14.3 X-ray and micro-CT evaluation

Radiography was performed for 4 weeks after the rabbits were anaesthetized with 3% pentobarbital (1 mL/kg). The right femurs with the implants were scanned by high-resolution micro-computed tomography (micro-CT; SkyScan 1176) at 60 kV and 400 μA with a 1 mm aluminum filter to determine the newly formed bone around the implants. The 2D and 3D high-resolution reconstructed images were generated by the software provided by the manufacturer.

1.14.4 Histopathological evaluation

H&E staining and Giemsa staining were used to assess bacterial contamination of soft tissue and bone around the implants after 2 and 4 weeks.[9-10] The histopathological analysis was carried out on a fluorescence microscope (IFM, Olympus, IX73) and Van Gieson's picro fuchsin staining was used to observe and visualize the mineralized bone tissue (red). The images were captured on a fluorescence microscope (IFM, Olympus, IX73).

1.15 Statistical analysis

All the quantitative data were analyzed by the one-way ANOVA and expressed as means ± standard deviations with n = 3. P values < 0.05 were considered statistically significant.

2. REFERENCES

(1) Vayssieres, L. Growth of Arrayed Nanorods and Nanowires of ZnO from Aqueous Solutions. *Adv. Mater.* **2003**, *15*, 464-466.

(2) Su, C. Y.; Hsueh, Y. C.; Kei, C. C.; Lin, C. T.; Perng, T. P. Fabrication of High-Activity Hybrid Pt@ZnO Catalyst on Carbon Cloth by Atomic Layer Deposition for Photoassisted Electro-Oxidation of Methanol. *J. Phys. Chem. C* **2013**, *117*, 11610-11618.

(3) Lee, H.; Dellatore, S. M.; Miller, W. M.; Messersmith, P. B. Mussel-Inspired Surface Chemistry for Multifunctional Coatings. *Science* **2007**, *318*, 426-430.

(4) Lee, J. S.; Murphy, W. L. Functionalizing Calcium Phosphate Biomaterials with Antibacterial Silver Particles. *Adv. Mater.* **2011**, *25*, 1173-1179.

(5) Xu, Z.; Li, M.; Li, X.; Liu, X.; Ma, F.; Wu, S.; Yeung, K. W. K.; Han, Y.; Chu, P. K. Antibacterial Activity of Silver Doped Titanate Nanowires on Ti Implants. *ACS Appl. Mater. Interfaces* **2016**, *8*, 16584-16594.

(6) Jin, G.; Qin, H.; Cao, H.; Qian, S.; Zhao, Y.; Peng, X.; Zhang, X.; Liu, X.; Chu, P. K. Synergistic Effects of Dual Zn/Ag Ion Implantation in Osteogenic Activity and Antibacterial Ability of Titanium. *Biomaterials* **2014**, *35*, 7699-7713.

(7) Ouyang, L.; Zhao, Y.; Jin, G.; Lu, T.; Li, J.; Qiao, Y.; Ning, C.; Zhang, X.; Chu, P. K.; Liu, X. Influence of Sulfur Content on Bone Formation and Antibacterial Ability of Sulfonated PEEK. *Biomaterials* **2016**, *83*, 115-126.

(8) Wu, T.; Tan, L.; Cheng, N.; Yan, Q.; Zhang, Y. F.; Liu, C. J.; Shi, B. PNIPAAM Modified Mesoporous Hydroxyapatite for Sustained Osteogenic Drug Release and Promoting Cell Attachment. *Mater. Sci. Eng., C* **2016,** *62*, 888-896.

(9) Wang, J.; Li, J.; Qian, S.; Guo, G.; Wang, Q.; Tang, J.; Shen, H.; Liu, X.; Zhang, X.; Chu, P. K. Antibacterial Surface Design of Titanium-Based Biomaterials for

Enhanced Bacteria-Killing and Cell-Assisting Functions Against Periprosthetic Joint Infection. *ACS Appl. Mater. Interfaces* **2016**, *8*, 11162–11178.

(10) Jin, G.; Qin, H.; Cao, H.; Qiao, Y.; Zhao, Y.; Peng, X.; Zhang, X.; Liu, X.; Chu, P. K. Zn/Ag Micro-Galvanic Couples Formed on Titanium and Osseointegration Effects in the Presence of *S. aureus*. *Biomaterials* **2015**, *65*, 22-31.

3. SUPPLEMENTARY FIGURES

Table S1. Abbreviations of different samples.

Sample	Abbreviation
Medical pure titanium	Ti
ZnO seed layer deposition by ALD on Ti	Ti-ZnOs
Hydrothermal growth of ZnO nanorod arrays on Ti	Ti-ZnO
Polydopamine coating on Ti-ZnO	Ti-ZnO/PDA
Covalent immobilization of RGDC peptide on Ti-ZnO/PDA	Ti-ZnO/PDA/RGDC

Table S2. Specific forward and reverse primer sequences of β-actin, ALP, RUNX2, and OCN genes.

Gene	Gene forward primer sequence (5'–3')	Reverse primer sequence (5'–3')
β-actin	TGCTATCCAGAAAACCCCTCAA	GCGGGTGGAACTGTGTTACG
ALP	GCCCTCCAGATCCTGACCAA	GCAGAGCCTGCTGGTCCTTA
RUNX2	TGCCCAGGCGTATTTCAG	TGCCTGGCTCTTCTTACTGAG
OCN	AGCAGCTTGGCCCAGACCTA	TAGCGCCGGAGTCTGTTCACTAC

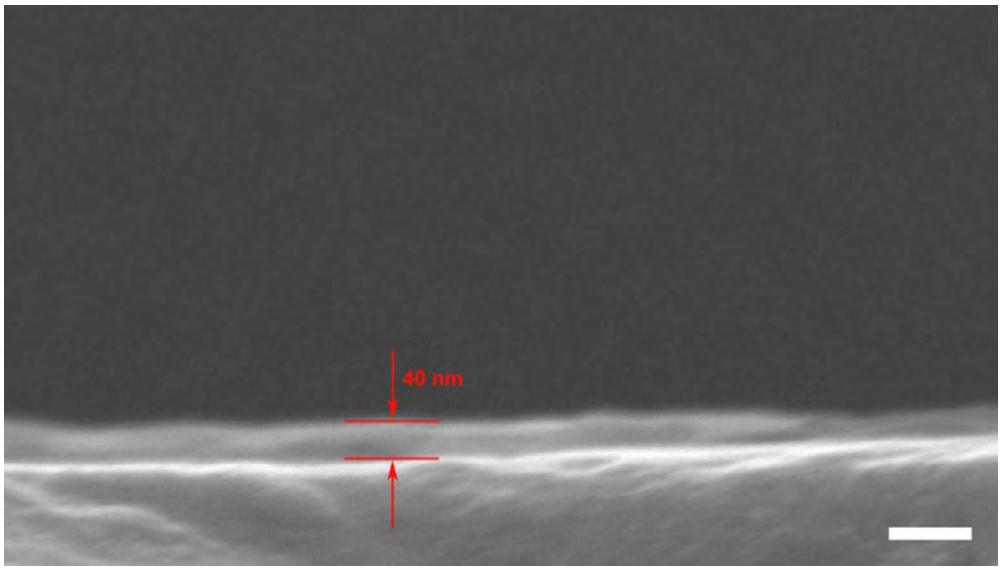

Figure S1. Cross-sectional view of Ti-ZnOs by SEM (scale bar = 100 nm).

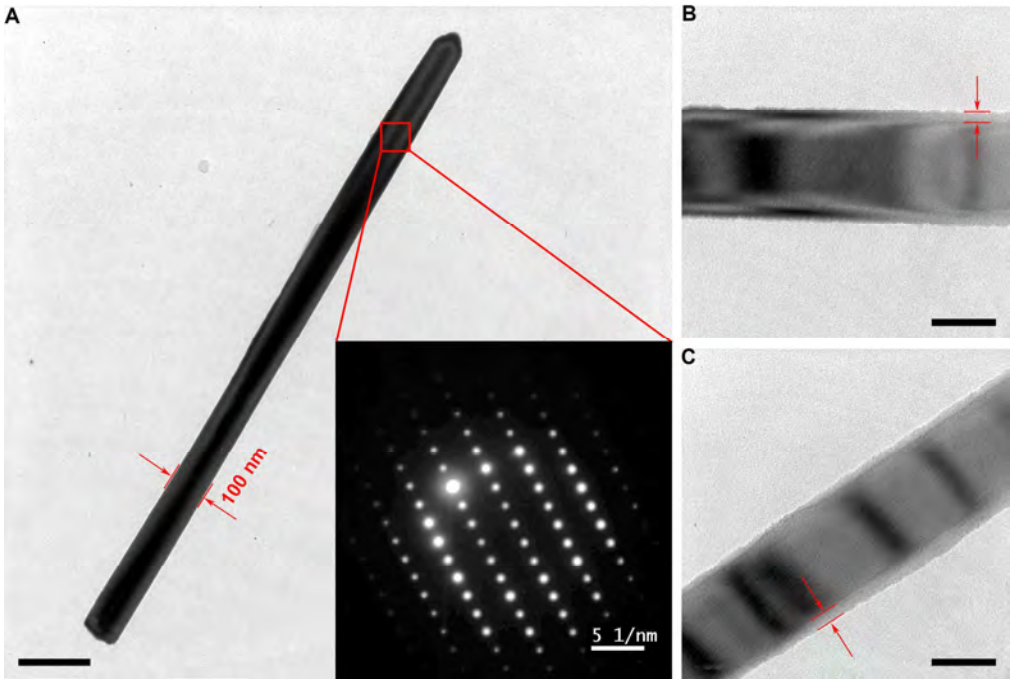

Figure S2. TEM images of (A) individual ZnO NR and corresponding SAED pattern (scale bars = 200 nm); (B) Ti-ZnO/PDA, (C) Ti-ZnO/PDA/RGDC (scale bars = 50 nm).

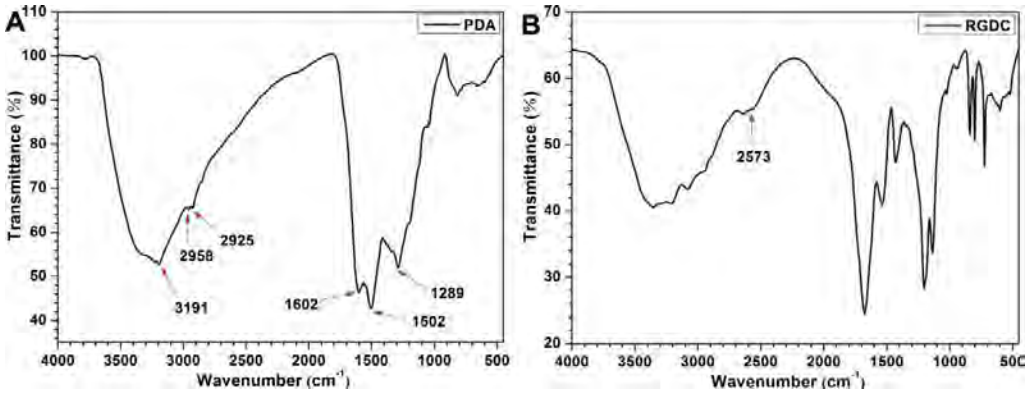

Figure S3. FTIR spectra of (A) PDA and (B) RGDC.

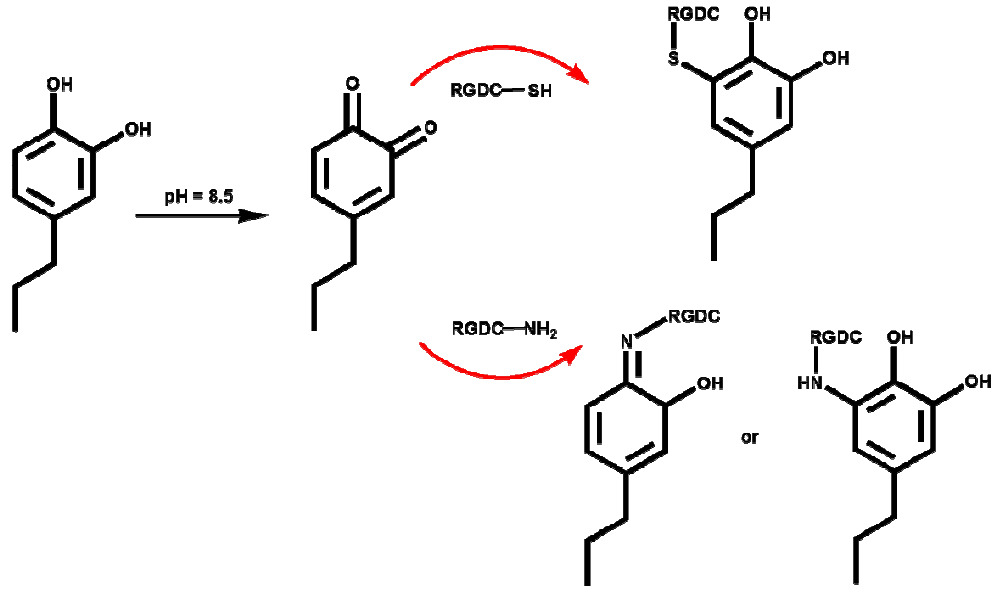

Figure S4. Covalent binding mechanism pertaining to covalent immobilization of RGDC peptide onto PDA.

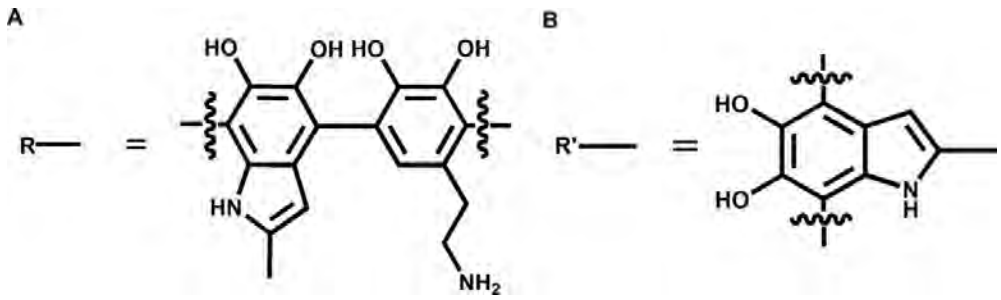

Figure S5. Chemical formula of (A) R group and (B) R' group.

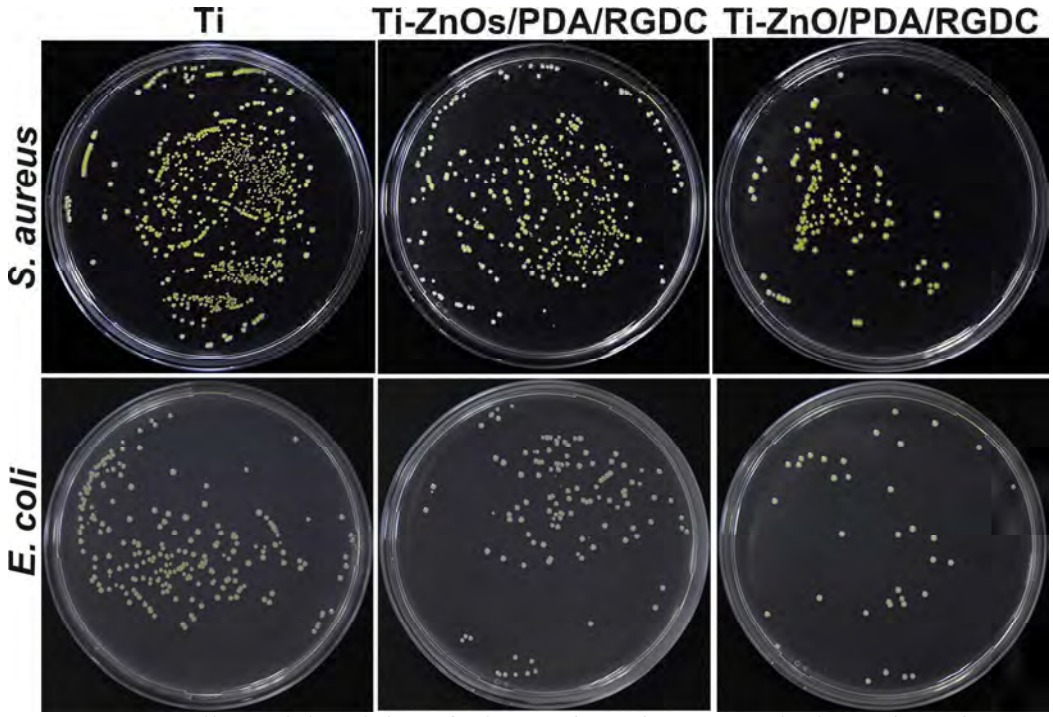

Figure S6. Antibacterial activity of Ti-ZnOs/PDA/RGDC and Ti-ZnO/PDA/RGDC through re-cultivated bacterial colonies on agar culture plates: *S. aureus* and *E. coli* seeded on various surfaces at a concentration of 10^7 CFU/mL.

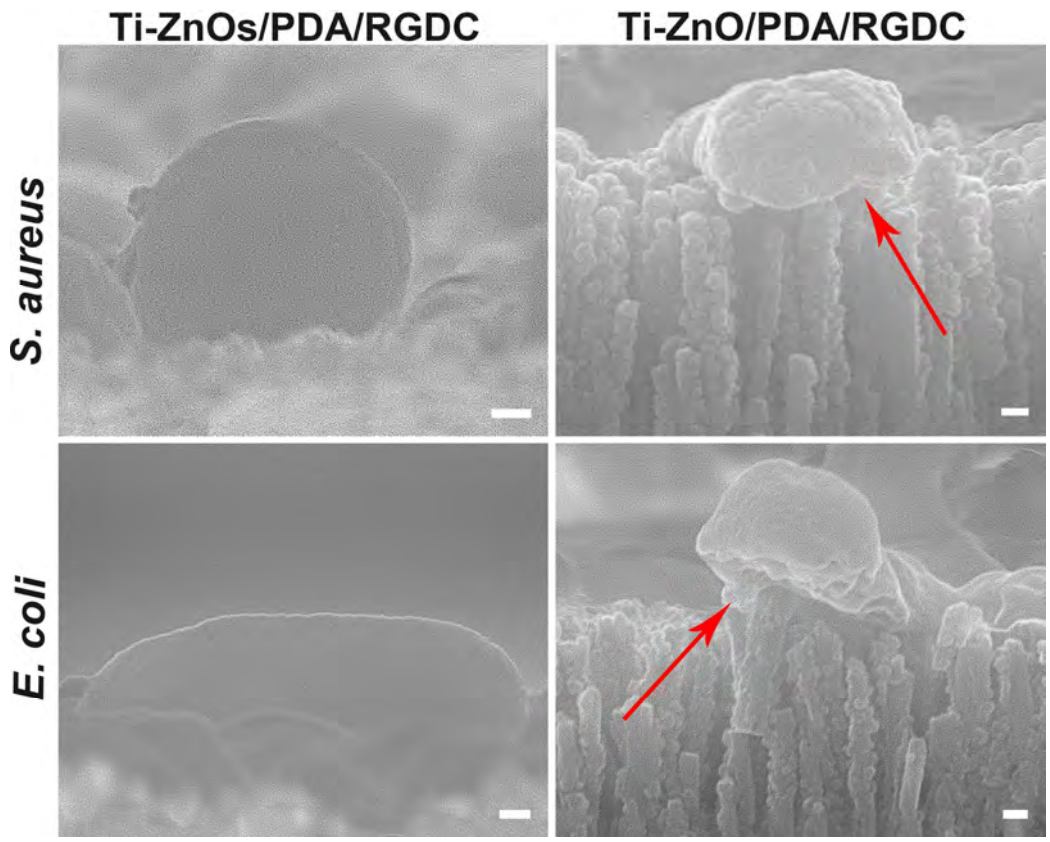

Figure S7. FE-SEM images of *S. aureus* and *E. coli* treated with Ti-ZnOs/PDA/RGDC and Ti-ZnO/PDA/RGDC (scale bars = 100 nm).

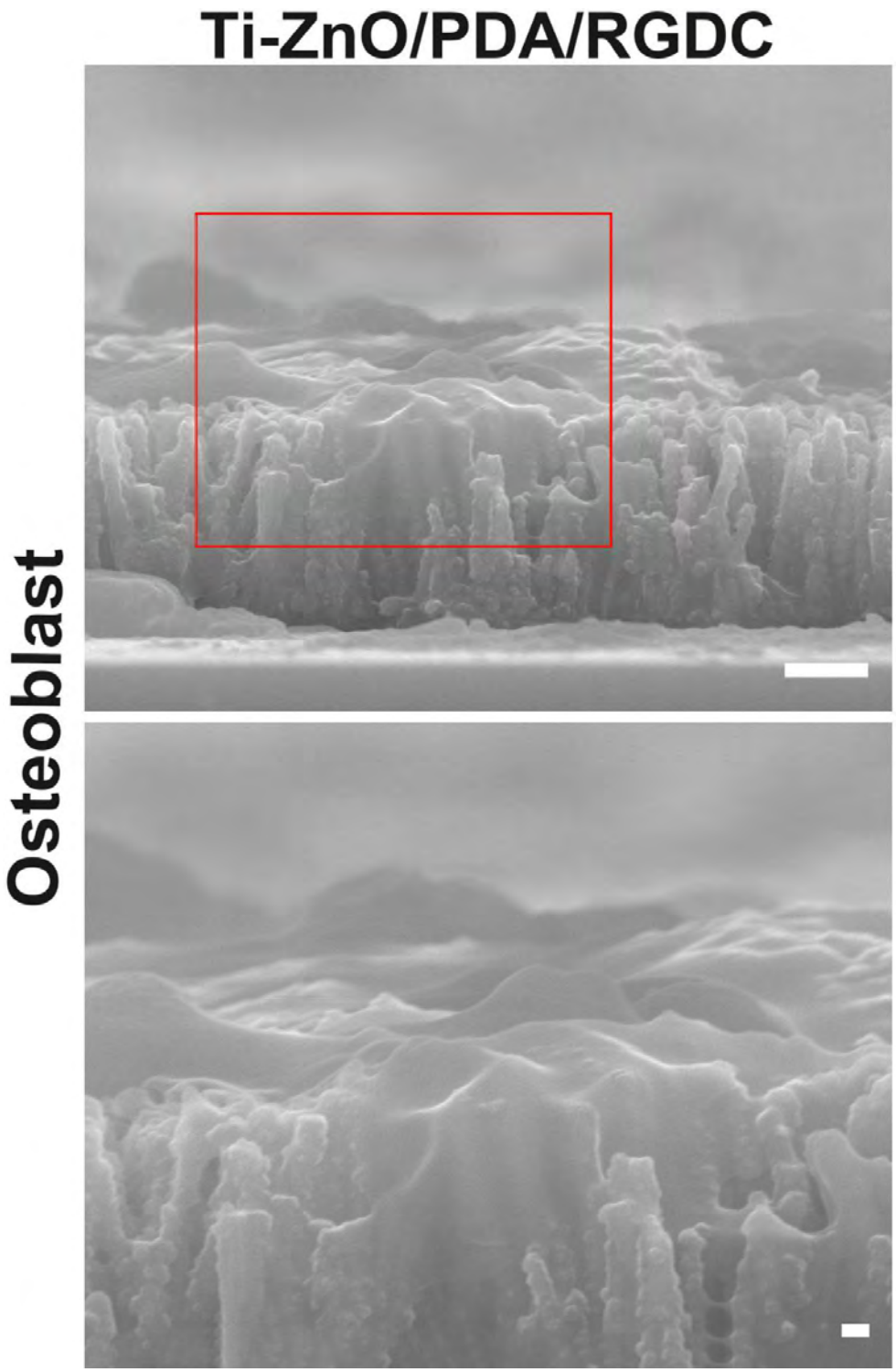

Figure S8. FE-SEM images of osteoblast treated with Ti-ZnO/PDA/RGDC (scale bars = 1 μm, 100 nm).

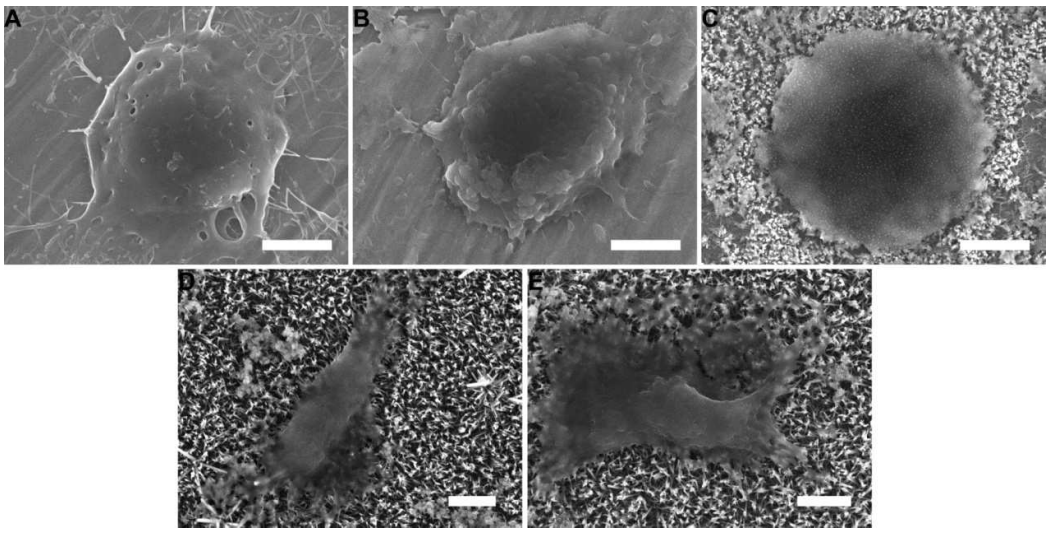

Figure S9. SEM images of MC3T3-E1 cells seeded on (A) Ti, (B) Ti-ZnOs, (C) Ti-ZnO, (D) Ti-ZnO/PDA, and (E) Ti-ZnO/PDA/RGDC after culturing for 12 h (scale bars = 5 μm).

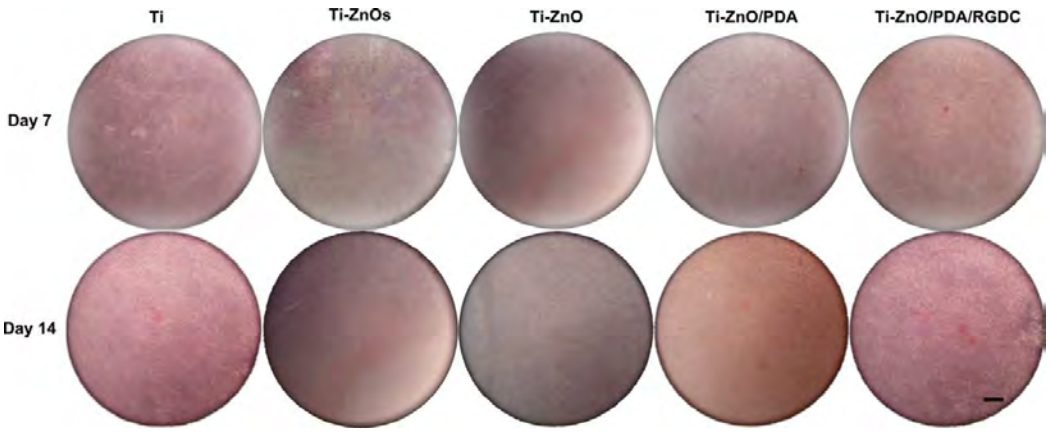

Figure S10. Alizarin Red staining of Ti, Ti-ZnOs, Ti-ZnO, Ti-ZnO/PDA, and Ti-ZnO/PDA/RGDC in the osteogenic medium for 7 and 14 days (scale bar = 200 μm).

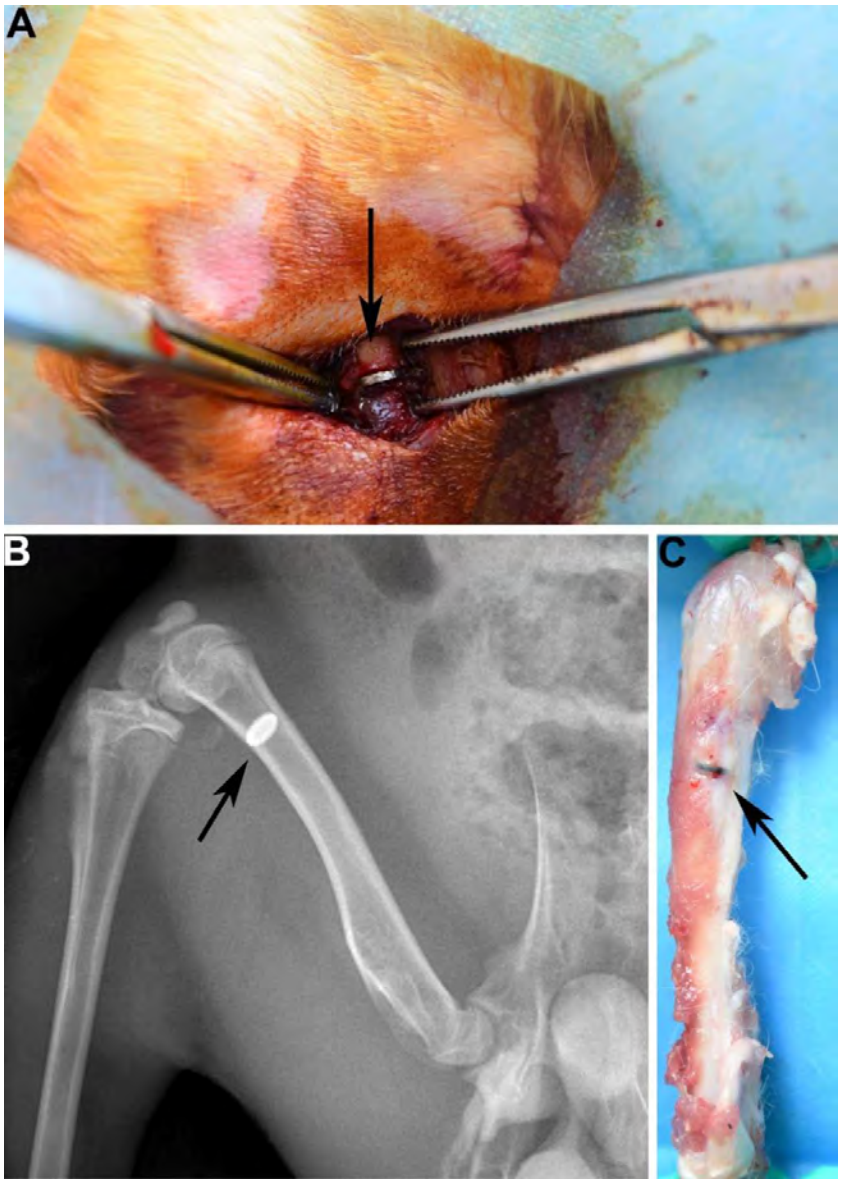

Figure S11. (A) Implantation of the Ti implant into the femur of adult male New Zealand white rabbits; (B) X-rays image; (C) Photograph of femur of rabbits inserted with the Ti implant 4 weeks after surgery.

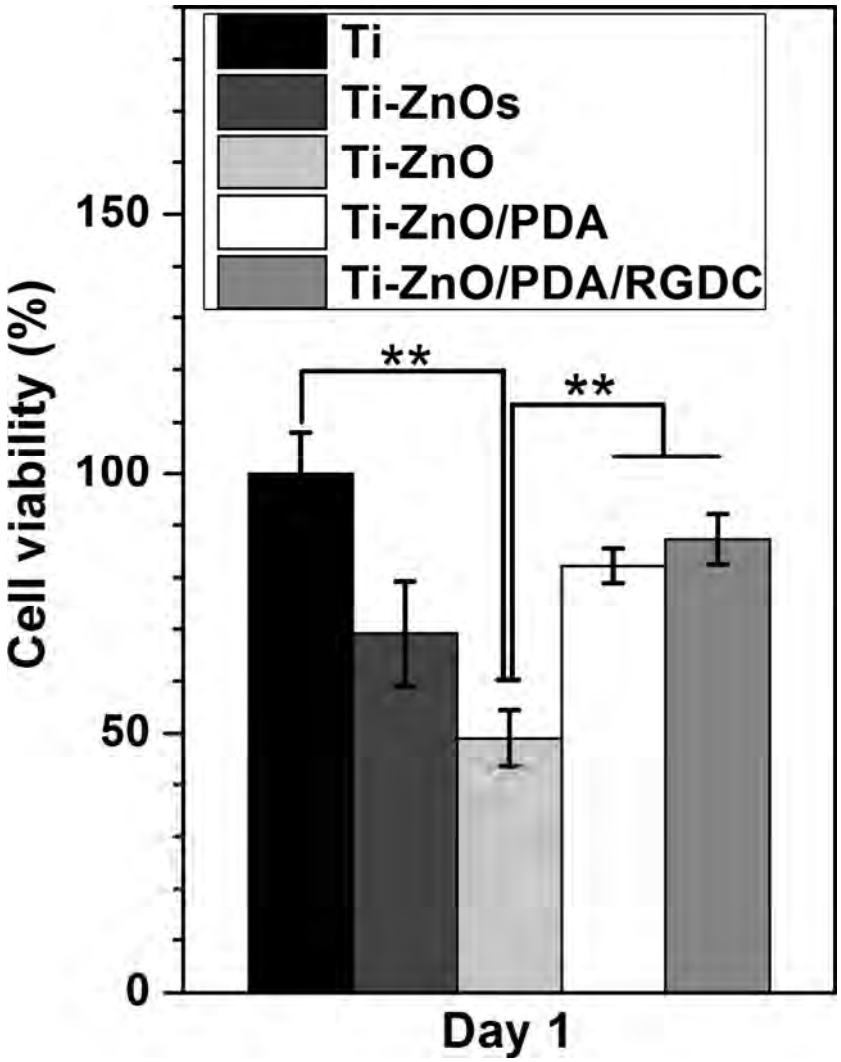

Figure S12. MTT assay of cells cultured in the corresponding extracted liquids of Ti, Ti-ZnOs, Ti-ZnO, Ti-ZnO/PDA, and Ti-ZnO/PDA/RGDC after one day release for another one day incubation. The error bars indicate means ± standard deviations: ***P* < 0.05 (t test).

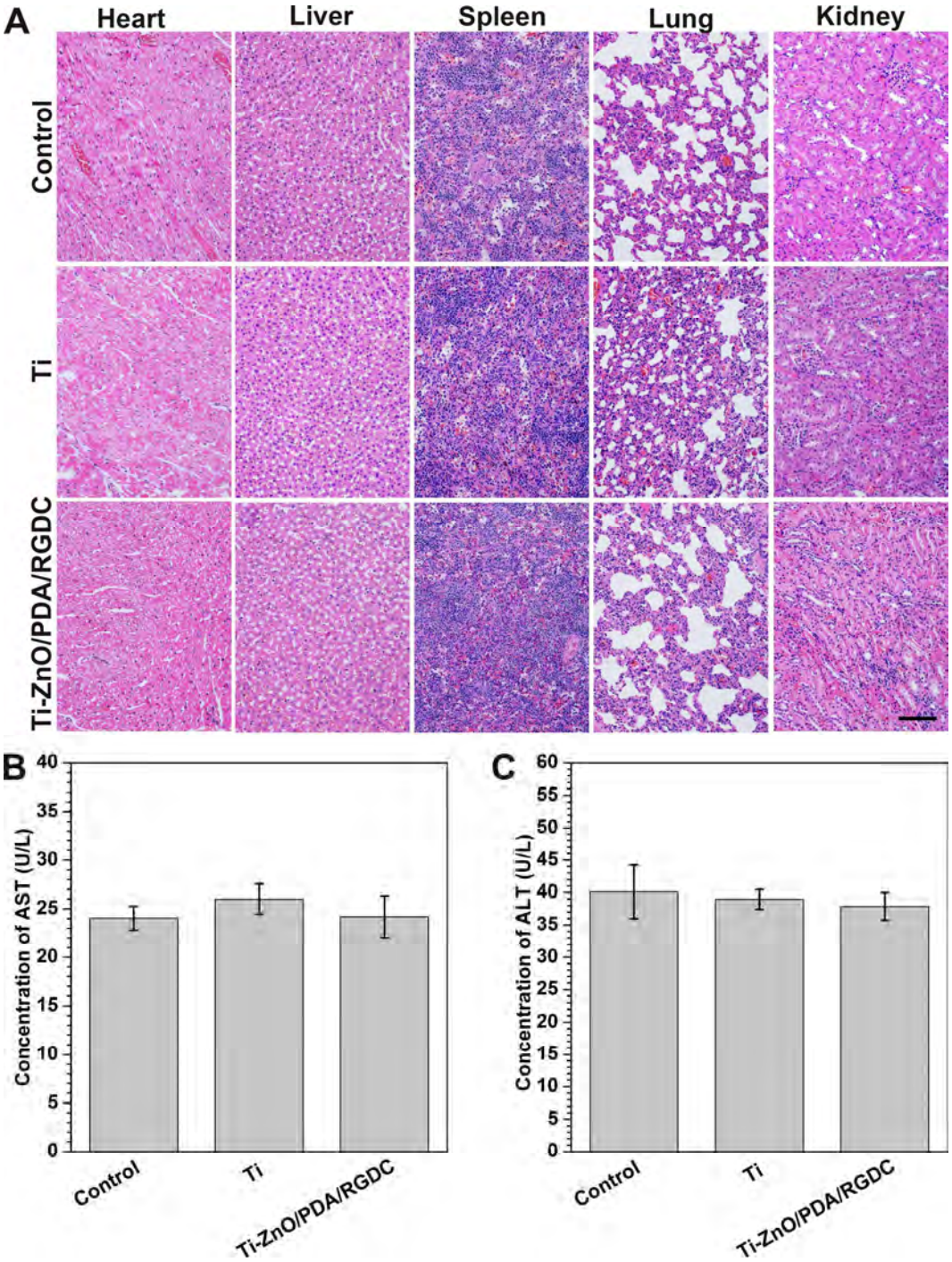

Figure S13. (A) Corresponding histological analyses of major organs including the liver, spleen, kidney, heart and lung by H&E staining (scale bar = 100 μm). (B) Serum AST and (C) ALT related to live enzyme after 2 weeks.